3

Improving the reliability of Fe- and S-XANES measurements in silicate glasses: correcting beam damage and identifying Fe-oxide nanolites in hydrous and anhydrous melt inclusions

7

8   Allan H. Lerner[1*], Michelle J. Muth[1], Paul J. Wallace[1], Antonio Lanzirotti[2], Matthew Newville[2],

9   Glenn A. Gaetani[3], Proteek Chowdhury[4], Rajdeep Dasgupta[5]

10

11   [1] Department of Earth Sciences, University of Oregon, Oregon 97403, USA

12   [2] Center for Advanced Radiation Sources, The University of Chicago, Illinois 60637, USA

13   [3] Department of Geology and Geophysics, Woods Hole Oceanographic Institution, Woods Hole,
14   Massachusetts 02543, USA

15   [4] Department of Earth and Planetary Sciences, University of California, Riverside, CA 92521, USA

16   [5] Department of Earth, Environmental, and Planetary Sciences, Rice University, Texas 77005, USA

17   [*] Corresponding author at: 1272 University of Oregon, Eugene, OR 97403, USA. *E-mail address:*
18   lerner.allan@gmail.com (A. H. Lerner).

19

20   **Highlights**

21   • Photo-oxidation during Fe-XANES analyses of glasses can be corrected by time-
22   dependent restorations to initial values

23   • Photo-reduction can occur rapidly during S-XANES analyses even in glasses that are
24   stable during Fe-XANES analysis

25   • Photo-reduction during S-XANES can be corrected by restoring S^{4+} to S^{6+} signal
26   intensities

27   • Fe-oxide nanolites in otherwise glassy melt inclusions can be identified by magnetite-like
28   features in Fe-XANES spectra

29   • Beam damage correction techniques enable accurate XANES measurements of damage-
30   susceptible glasses and melt inclusions

31 **Abstract**

32   The redox state of silicate melts influences crystallization, element partitioning, and

33 degassing behavior. Synchrotron-based micro-X-ray absorption near edge structure (µXANES)

34 spectroscopy has emerged as a powerful tool for determining redox conditions through the direct

35 measurement of speciation of multivalent elements such as iron and sulfur in silicate glasses. In

36 particular, the high spatial resolution afforded by synchrotron µXANES makes it one of the few

37 techniques available for determining redox conditions in melt inclusions, which can provide

38 insights into pre-eruptive melt properties. However, the small size of melt inclusions, the deep

39 penetration of X-rays, and irradiation-induced beam damage make µXANES measurements in

40 melt inclusions challenging. Here we present data that show rapid Fe- and S-µXANES beam

41 damage in experimental glasses, mid-ocean ridge basalt glasses, and olivine-hosted melt

42 inclusions from the southern Cascade arc and Kīlauea Volcano and develop approaches to

43 recognize and correct for beam damage through repeated rapid analyses. By applying a time-

44 dependent correction to a series of rapid measurements (~82 s/scan) of Fe-µXANES pre-edge

45 centroid positions, irradiation-induced photo-oxidation (Fe^{2+} to Fe^{3+}) can be corrected back to

46 undamaged initial $Fe^{3+}/\Sigma Fe$ even in damage-susceptible hydrous glasses. Using this beam

47 damage correction technique, hydrous basaltic melt inclusions from the southern Cascades have

48 $Fe^{3+}/\Sigma Fe$ that is ~0.036 lower (corresponding to -0.5 log units lower oxygen fugacity) than would

49 have been indicated by standard Fe-µXANES measurements. Repeated, rapid analyses (150 –

50 300 s/scan) were used to identify S-µXANES beam damage (photo-reduction of S^{6+} to S^{4+}),

51 which was corrected with a peak fitting method to restore initial $S^{6+}/\Sigma S$. We observe that S-

52 µXANES beam damage can occur rapidly even in low-H_2O mid-ocean ridge basaltic glasses and

53 melt inclusions from Kīlauea Volcano, which are otherwise stable during even prolonged Fe-

54 µXANES analyses. By mitigating and correcting for sulfur photo-reduction, we conclude that

55 some mid-ocean ridge basaltic glasses contain 0.08 – 0.09 $S^{6+}/\Sigma S$, which is more sulfate than

56 might be expected based on the reduced oxidation state of these glasses (near the fayalite-

57 magnetite-quartz oxygen buffer). Using beam damage identification and correction techniques,

58 the valence states of iron and sulfur can be accurately measured even in beam damage-

59 susceptible glasses and melt inclusions. Finally, using Fe-µXANES, we demonstrate the

60 presence of Fe-oxide nanolites within otherwise glassy, naturally quenched melt inclusions,

61 which can complicate determination of iron valence state in affected glasses.

62

63   **Key words:** XANES; Beam Damage; Nanolites; Sulfur; Iron; Melt Inclusions

64

1.1 Introduction

66   Synchrotron-based micro-X-ray absorption near edge structure (µXANES) spectroscopy

67   has become a valuable petrologic tool for *in situ* determination of the valence state and molecular

68   complexing of redox-sensitive elements in magmatic minerals and glasses (see review by Sutton

69   et al., 2020). In particular, Fe- and S-µXANES have been applied to quenched volcanic glasses

70   to advance our understanding of magmatic oxygen fugacity (fO$_2$) and complexing of species in

71   glasses from Earth's mid-ocean ridges, hotspots, and volcanic arcs (Bonnin-Mosbah et al., 2001,

72   2002; Wilke et al., 2006; Berry et al., 2008; Kelley and Cottrell, 2009; Cottrell and Kelley, 2011;

73   Brounce et al., 2014, 2017; Dyar et al., 2016; Lanzirotti et al., 2019; Moussallam et al., 2019;

74   Sutton et al., 2020), as well as in igneous material from lunar and Martian samples (Righter et

75   al., 2013; McCanta et al., 2017, 2019). The fO$_2$ of magmas exerts a major control on mineral

76   stability and thereby the differentiation paths of magmas (Osborn, 1959; Kelley and Cottrell,

77   2012), including the behavior of important ore-forming species (e.g. Cr, Cu, Fe, Ti; Papike et al.,

78   2016; Lanzirotti et al., 2019; Sutton et al., 2020). Additionally, fO$_2$ can significantly affect the

79   solubility and degassing of multivalent volatiles (e.g., S, C) (Jugo, 2009; Jugo et al., 2010; de

80   Moor et al., 2013; Jégo and Dasgupta, 2014; Moussallam et al., 2014, 2016; Helz et al., 2017;

81   Head et al., 2018). A well-established approach to determining melt fO$_2$ is by measuring

82   Fe^{3+}/ΣFe in quenched glasses (e.g., Kress and Carmichael, 1991; Borisov et al., 2018; O'Neill et

83   al., 2018).

84   Iron occurs as both Fe^{2+} and Fe^{3+} in most terrestrial melts, and as Fe^{2+} or Fe^0 in strongly

85   reduced melts below the IW buffer (generally extraterrestrial) (Schreiber et al., 1987). Fe-

86   XANES allows the mean valence state of iron in minerals and silicate glasses to be determined

87   based on spectral features at energies below the iron absorption edge (pre-edge features), while

88   higher energy features inform iron bonding coordination in minerals (e.g., Waychunas et al.,

89   1983; Bajt et al., 1994; Wilke et al., 2001, 2004, 2006; Berry et al., 2003, 2008; Farges et al.,

90   2004; Cottrell et al., 2009). Fe-XANES pre-edge features in glasses are specifically sensitive to

91   valence state, and measured spectra can therefore be related to glass Fe^{3+}/ΣFe by comparison to

92   suites of glass standards synthesized under controlled redox conditions and analyzed using

93   Mössbauer spectroscopy (e.g., Berry et al., 2003; Wilke et al., 2004; Cottrell et al., 2009).

94   Several published calibrations relate measured Fe-XANES spectral centroid position associated

95   with Fe^{2+} and Fe^{3+} pre-edge peaks to $Fe^{3+}/\Sigma Fe$ in silicate glasses (Galoisy et al., 2001; Bonnin-

96   Mosbah et al., 2001; Berry et al., 2003; Wilke et al., 2004, 2007; Cottrell et al., 2009; Dauphas et

97   al., 2014; Zhang et al., 2016, 2018; Fiege et al., 2017). Other recent calibrations have used

98   multivariate analysis of the entire Fe-XANES spectrum to determine iron valence in standard

99   glasses measured by Mössbauer (Shorttle et al., 2015; Dyar et al., 2016).

100   Sulfur in silicate melts dominantly occurs as S^{2-} or S^{6+} (Carroll and Rutherford, 1988;

101   Wilke et al., 2008). The transition between S^{2-} and S^{6+} species in silicate melts occurs over a

102   relatively narrow fO$_2$ range near the Ni-NiO buffer (Carroll and Rutherford, 1988; Jugo et al.,

103   2010; Botcharnikov et al., 2011), although there is evidence that this transition is dependent on

104   pressure, temperature, and melt composition (Baker and Moretti, 2011; Klimm et al., 2012a;

105   Fiege et al., 2014; Masotta and Keppler, 2015; Matjuschkin et al., 2016; Nash et al., 2019). S-

106   XANES has been used to quantify the $S^{6+}/\Sigma S$ in glasses by fitting the relative intensity of

107   absorption peaks for sulfide and sulfate species that occur at ~2475 – 2479 and ~2481 – 2483

108   eV, respectively (Paris et al., 2001; Métrich et al., 2002, 2009; Bonnin-Mosbah et al., 2002; Fleet

109   et al., 2005; Jugo et al., 2010). These two sulfur species generally have distinct spectral

110   absorbance features when present in silicate glasses. Based on melt composition and cooling

111   history, reduced sulfur can also occur in a variety of metal-sulfide complexes, each of which has

112   particular identifiable spectroscopic features (Li et al., 1995; Bonnin-Mosbah et al., 2002; Fleet

113   et al., 2005; Head et al., 2018).

114   Fe- and S-XANES are particularly powerful techniques for investigating redox conditions

115   of melt inclusions (MI), which are small parcels of quenched glass formed from melt entrapped

116   within growing crystals. Melt inclusions are useful because they can preserve information on

117   volatile concentrations and melt diversity that is otherwise lost during magma mixing, ascent,

118   and eruption (Kent, 2008; Métrich and Wallace, 2008; Wallace et al., 2021). Melt inclusions in

119   many systems of petrologic interest have mean diameters of 10 – 100 μm. The small size of MI

120   leaves μXANES (hereafter XANES) as one of the few techniques suitable for *in situ*

121   measurements of element speciation (i.e., valence state and molecular coordination) within MI.

122   Of course, inferring magma redox state from iron and sulfur valence in quenched glasses

123   requires accurate XANES measurements. The large penetrative depths of high-energy X-rays

124   and oblique incident beam trajectories at many analytical facilities require careful sample

125   preparation and analytical strategies to avoid signal contamination during Fe- and S-XANES

126   measurements of MI and matrix glasses (Figure 1). It has also been recognized that many glass

127   compositions are susceptible to X-ray induced changes in iron and sulfur speciation during

128   analysis (i.e., beam damage) (Wilke et al., 2008; Métrich et al., 2009; Gonçalves Ferreira et al.,

129   2013; Moussallam et al., 2014, 2019; Cottrell et al., 2018; Hughes et al., 2020). Although Fe-

130   XANES measurements of nominally anhydrous basaltic and rhyolitic glasses are observed to be

131   reproducible over a broad range of incident X-ray fluxes (Cottrell et al., 2009), hydrous volcanic

132   glasses, particularly basaltic compositions, have been observed to undergo rapid oxidation of

133   Fe^{2+} to Fe^{3+} with progressive irradiation (Cottrell et al., 2018; Moussallam et al., 2019). The

134   exact mechanisms of iron photo-oxidation are not fully understood, but involve the production of

135   photoelectrons and the local accumulation of charge in non-conductive materials, which alters

136   the electron state of multivalent elements. The ensuing redox exchanges within glasses are

137   accelerated by O-H volatilization or migration (Cottrell et al., 2018).

138   S-XANES measurements in silicate glasses have also been observed to undergo beam-

139   induced changes in speciation, typically with S^{6+} being reduced to S^{4+} during progressive X-ray

140   irradiation (Wilke et al., 2008; Métrich et al., 2009). Strategies to mitigate beam damage during

141   Fe- and S-XANES measurements include reducing X-ray flux density (photon flux/analytical

142   area) by using defocused beams, continually moving the sample during analysis, and/or

143   decreasing incident photon flux (Wilke et al., 2008; Métrich et al., 2009; Klimm et al., 2012a;

144   Brounce et al., 2017; Cottrell et al., 2018; Moussallam et al., 2019). Spatially resolved XANES

145   beamlines are available at a number of synchrotron light sources worldwide with incident X-ray

146   intensities ranging from $10^8 – 10^{12}$ photons/s (Sutton et al., 2020), where higher X-ray fluxes

147   shorten analysis time by providing lower detection limits, but amplify beam damage concerns.

148   Many of these approaches to lessen beam damage are challenging to apply to MI owing

149   to their small sizes. Smaller MI require more focused beam diameters to avoid contamination by

150   the host-phase, but are thereby subject to higher photon densities and thus possible beam damage

151   (e.g., Gaborieau et al., 2020; Tassara et al., 2020). Melt inclusions are often targeted for

152   petrological investigation specifically because they can retain magmatic volatiles that are

153 otherwise lost from the external magma during ascent and degassing (Kent, 2008; Métrich and

154 Wallace, 2008). However, silicate glasses with high H_2O content have been observed to undergo

155 larger changes in iron (and potentially sulfur) speciation during irradiation than what is observed

156 in anhydrous silicate glasses (Cottrell et al., 2018; Moussallam et al., 2019). Hydrous MI may

157 also be susceptible to the formation of nanolite crystals during quenching (Danyushevsky et al.,

158 2002; Di Genova et al., 2018), which may lead to spurious interpretation of XANES spectra.

159 These combined properties make it particularly challenging to apply XANES oxybarometry

160 methods to the analysis of MI from volcanic arc environments, which tend to be both small and

161 H_2O-rich.

162   For these more challenging MI, it is beneficial to develop XANES approaches that both

163 minimize changes in elemental speciation during irradiation and correct for changes that do

164 occur. Applying generalized corrections to datasets is not ideal because differences in glass

165 compositions and H_2O contents (e.g., caused by variable diffusive H^+ loss from MI before

166 quenching) can lead to different MI susceptibilities to beam damage within the same deposit or

167 even within the same host mineral.

168   In this study, we present techniques that aid in recognizing X-ray--induced changes in

169 iron and sulfur valence in volcanic glasses and MI that result from XANES analysis. We then

170 propose new time-dependent corrections for beam damage that does occur. For S-XANES, we

171 also introduce a new spectral fitting approach that may better account for reduction of S^{6+} to S^{4+}

172 during analysis. Finally, we present a method to identify the presence of Fe-oxide nanolites in

173 MI during Fe-XANES analysis. Collectively, these methods enable reliable quantification of iron

174 and sulfur valence, and thereby melt redox state, from small and/or beam damage-susceptible

175 glasses and MI.

176

2.1 XANES analysis of melt inclusions

2.1.1 Geometric considerations

179   At the Fe *K*-edge, the characteristic 1/e X-ray absorption depth in basaltic glass is $\approx$ 40

180 μm (Elam et al., 2002), and 120 μm ($1/e^3$) thick glass is therefore required for 95% absorption of

181 X-rays during Fe-XANES measurements. X-ray absorption by Fe-bearing inclusions or

182 crystalline host phases that may be present within the analytical path will be mixed with the

183   signal of the targeted glass. This is a particular problem for analyzing MI, as MI are often less

184   than 100 μm thick. Consequently, most MI must be doubly intersected for Fe-XANES analysis

185   to avoid signal contamination from the host mineral. A further complication in XANES

186   measurements of MI, particularly for highly penetrative Fe-XANES analyses, is that many

187   μXANES beamline configurations utilize a ~45° slant geometry of incoming X-ray beam in

188   fluorescence operating modes. The inclined incidence angle means that as wafer thickness

189   increases in the beam direction, progressively wider doubly-intersected MI areas are needed to

190   keep the analytical path free of mineral contamination (Figure 1). Throughout the X-ray

191   penetration volume, the minimum required doubly-intersected MI dimensions for a host-free

192   glass measurement are roughly equal to MI thickness plus the beam diameter size (assuming a

193   cylindrical doubly-intersected MI area). This requires MI to be either sufficiently wide or ground

194   very thin for clean glass analyses using high energy X-rays (e.g., Fe-XANES, V-XANES, Cu-

195   XANES). Thus, small MI in olivine and other Fe-bearing phases can be challenging to measure

196   for Fe-XANES. Even for analyses of MI in phases that have low, but non-zero, Fe-

197   concentrations (e.g., feldspars), the high penetrative depth of Fe-XANES can excite a large

198   volume of the host phase, so that the host contribution to the Fe-XANES signal may be

199   significant. This issue is of particular concern for small MI and for glass compositions with

200   relatively low Fe-contents, such as dacites and rhyolites. At the lower energy S *K*-edge (~2500

201   eV), X-rays are more strongly attenuated, with the 1/e X-ray absorption depth in basaltic glass

202   only ~5 μm. Consequently, 95% of the S-XANES X-ray absorption occurs within the upper 15

203   μm and most of these geometric concerns are accordingly lessened (Figure 1A).

204

205
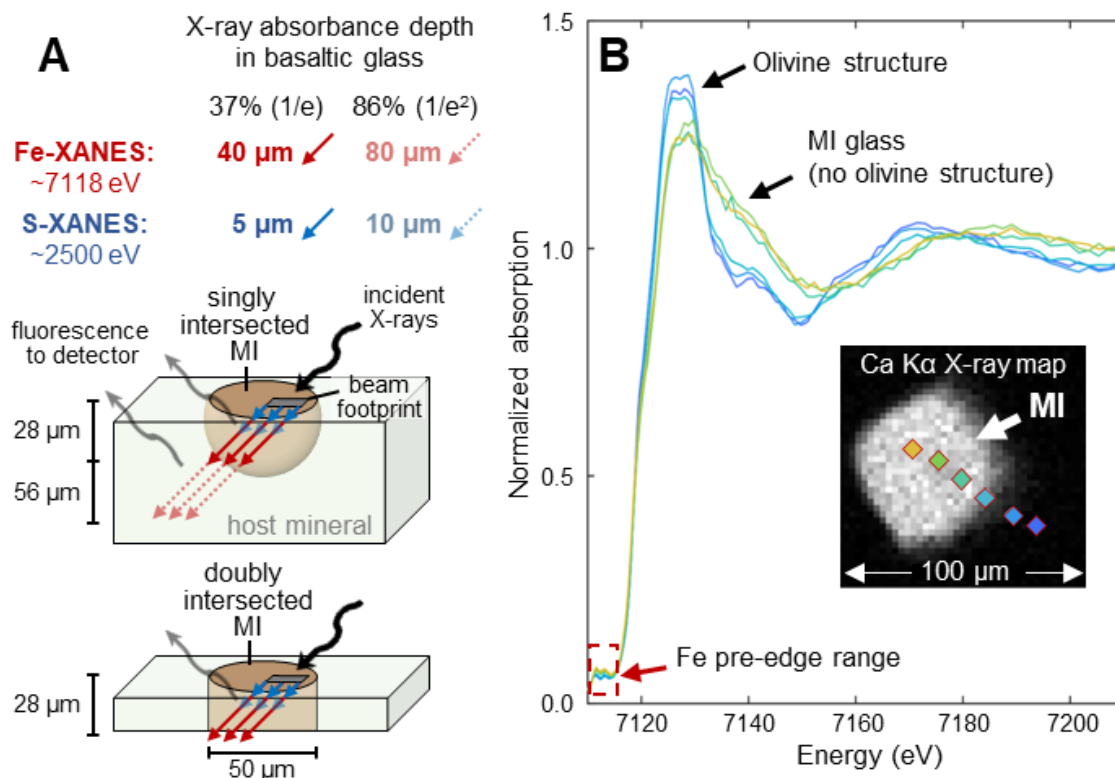
Figure 1. *(A)* Schematic analytical XANES geometry of a 50 μm diameter melt inclusion (MI) (brown) analyzed with a 20×20 μm X-ray beam. For many XANES fluorescence measurements, the X-ray beam (black arrow) is ~45° incident to the sample surface and the sample fluorescent energy (gray arrows) is measured at 45° in the opposite direction. Depending on the penetration depth of the X-ray energy being used, the beam may interact with substantial host mineral both laterally and at depth, leading to mineral-contaminated spectra. For Fe-XANES (red arrows), 37% and 86% of the X-ray signal are absorbed in 40 and 80 μm hypotenuse paths through basaltic glass (28 and 56 μm vertical thicknesses), requiring the MI be both doubly intersected and sufficiently wide to avoid host mineral contamination. S-XANES X-ray energies are much less penetrating (blue arrows), so MI geometry and thickness concerns are lessened. *(B)* A series of Fe-XANES measurements of a doubly-intersected olivine-hosted MI from the southern Cascades (BORG-1_37, Table 1) showing a traverse from within the MI into the olivine-host, demonstrating the difference in absorption edge shape between analyses of glass and of olivine. Measurement locations are shown atop a Ca Kα X-ray map (inset), with symbol colors matching the shown spectra.

2.1.2 Analytical details and sample descriptions

Fe- and S-XANES measurements were conducted on a variety of volcanic and experimental silicate glasses at GSECARS beamline 13-ID-E at Argonne National Laboratory's (Illinois, USA) Advanced Photon Source (APS), a third generation synchrotron light source (Sutton et al., 2017). Details of the 13-ID-E beamline configuration are described in Head et al.

228   (2018) and are consistent with measurements conducted here, except for differences in photon

229   flux and analytical times described below.

230   To account for differences in monochromator calibrations between synchrotron facilities,

231   a set of standards (minerals, metal foils, synthetic glasses) were measured at the onset of each

232   analytical session to determine the appropriate energy offset to apply to Fe- and S-XANES

233   oxybarometer calibration curves relative to reference energy fitting ranges (details below). At

234   beamline 13-ID-E, the lattice constants for the monochromator Si(111) and Si(311) crystals are

235   calculated from reference foils measured throughout the analyzable energy range of the crystals,

236   and provide excellent consistency with absorption edge energies determined by Kraft et al.

237   (1996). The 13-ID-E beamline has excellent reproducibility in measured reference materials over

238   the course of standard two to three-day measurement periods and therefore no within-session

239   drift corrections were applied during either Fe- or S-XANES measurements. Prior to each

240   XANES analysis, an X-ray map was made by rapidly rastering across the sample to identify

241   areas in MI and other glass targets that were free of host mineral and microlite crystals in the

242   beam path. The X-ray beam was then turned off to prevent any further unnecessary beam

243   interaction with the glasses until XANES measurements began.

244   Analyzed samples include doubly-intersected MI and matrix glasses mounted on Fe-free

245   glass rounds and thin sections. Samples were embedded in CrystalBond®, EpoThin® epoxy, or

246   thin section resin. All bonding material and glass substrates were analyzed to confirm that they

247   contained only trace iron and had negligible contribution to Fe-XANES signals. The bonding

248   materials did contain substantial S, but the low energy X-rays for S-XANES measurements are

249   fully absorbed within a ~20 μm path within basaltic glasses (15 μm vertical path with 45º

250   incident beam angle, Figure 1A). All analyzed MI and matrix glass areas are thicker than 20 μm,

251   so that the bonding materials contributed no appreciable signal to S-XANES measurements. We

252   also analyzed singly intersected experimental glass charges, where glass thicknesses of multiple

253   mm fully absorbed X-rays at both Fe- and S-$K\alpha$ energies so that contamination from the capsule

254   material was insignificant. In experimental glass charges, care was taken to analyze only crystal-

255   poor glass areas and to avoid measurements near capsule edges.

256

257

258

9

259   **Table 1**: Experimental and natural glasses analyzed by Fe- and S-XANES in this study.

Sample, composition	H_2O (wt%)	Fe-XANES beam damage susceptibility index (Φ)*	XANES analysis type	$Fe^{3+}/\Sigma Fe$ and $S^{6+}/\Sigma S$ ranges**	Photon density (photons/s/μm^2); observed beam damage***
CAB-47: experimental basaltic glass. 1250 °C, 1.3 GPa, minor phenocrysts (Weaver et al., 2011; this study)	5.5	1.6	Fe-XANES (+ photo-oxidation time series tests) S concentration too low for S-XANES	0.13 Fe^{3+}	Fe-XANES: $1 - 1.5 \times 10^8$: high $2 - 4 \times 10^7$: high $6 - 9 \times 10^6$: med
CAB-33: experimental basaltic glass. 1225 °C, 1.7 GPa, phenocryst-free, but Fe-oxide nanolite spectral signature (Weaver et al., 2011; this study)	7.2	1.8	Fe-XANES (+ photo-oxidation time series tests) S concentration too low for S-XANES	Fe-oxide nanolites present	Fe-XANES: $2 - 4 \times 10^7$: severe $6 - 9 \times 10^6$: high
P2-F: Mono Craters obsidian pyroclast with <0.1% microlites (Barnes et al., 2014; Watkins et al., 2017; this study)	2.0 – 2.3	-	Fe photo-oxidation time series tests	-	Fe-XANES: $1 - 1.5 \times 10^8$: med $2 - 4 \times 10^7$: slight
G466: experimental basalt glass. 1300 °C, 2 GPa, minor clinopyroxene + anhydrite (Chowdhury and Dasgupta, 2019; this study)	6.5	-	S-XANES	1.0 S^{6+}	S-XANES: 5×10^9: severe 2×10^8: high 5×10^7: med 8×10^6: slight
G479: experimental basalt glass. 1300 °C, 1.5 GPa, minor anhydrite (Chowdhury and Dasgupta, 2019; this study)	8.9	-	S-XANES	1.0 S^{6+}	S-XANES: 8×10^6: slight
MORB glasses: **VG-2** (Jarosewich et al., 1980; Rose and Brown, 2017; Zhang et al., 2018; this study) **JDF-46N** (Fiege et al., 2014; this study) **ALV892-1** (Fiege et al., 2014; this study)	<0.1	~0.01	S-XANES	~0.15 Fe^{3+} 0.04 – 0.08 S^{6+}	S-XANES: 1×10^{10}: severe 4.5×10^8: high 1×10^8: med 6.5×10^6: slight
KE62-3293S: Kīlauea 2018 basaltic pumice MI and matrix glass (Lerner et al., in revision; this study)	0.1 – 0.3	0.1	Fe-XANES S-XANES	0.13 – 0.18 Fe^{3+} 0.03 – 0.25 S^{6+}	Fe-XANES: $2 - 4 \times 10^7$: none S-XANES: 2×10^8: med 5×10^7: slight 8×10^6: none
KE62-3315F: Kīlauea 2018 littoral bomb MI and matrix glass (Lerner et al., in revision; this study)	0.1 – 0.2	0.03	Fe-XANES S-XANES	0.20 – 0.34 Fe^{3+} 0.68 – 0.96 S^{6+}	Fe-XANES: $2 - 4 \times 10^7$: none S-XANES: 5×10^7: high 8×10^6: slight
Lassen (southern Cascades): olivine-hosted MI **BRM, BBL, BORG** (Muth and Wallace, 2021; this study)	0.3 – 3.7	0.1 – 0.7	Fe-XANES S-XANES	0.14 – 0.31 Fe^{3+} 0.20 – 0.98 S^{6+}	Fe-XANES: $2 - 4 \times 10^7$: med S-XANES: 5×10^7: med 8×10^6: slight
Augustine 2006: **AUG_308** – low silica andesite tephra; **AUG_HSA2** – high silica andesite tephra (Lerner, 2020; this study)	1.0 – 4.0	0.2	Fe-XANES	0.39 – 0.44 Fe^{3+} (in glasses with no Fe-oxide nanolites)	Fe-XANES: $1 - 1.5 \times 10^8$: slight to none
Cerro Negro: olivine-hosted MI (Gaetani et al., 2012; this study)	3.0 – 4.0	0.5	Fe-XANES	Fe-oxide nanolites present	Fe-XANES: not tracked with repeat scans

* Fe-XANES beam damage susceptibility index (Cottrell et al., 2018): $XH_2O*2XFeO/XFe_2O_3$, calculated using molar fractions and Fe^{2+}/Fe^{3+} from time-zero interpolated Fe-XANES measurements. Full glass compositions are presented in the **Data supplement**.
** $Fe^{3+}/\Sigma Fe$ and $S^{6+}/\Sigma S$ ranges for beam damage corrected Fe- and S-XANES analyses. XANES spectra and results are presented in the **Data supplement.**
***Incident photon flux was ~3 – 5×10^9 photons/s for Fe-XANES, and ~1 – 40×10^9 photons/s for S-XANES. Analysis footprint sizes ranged from 2×2, 5×5, 10×10, 20×20, and 50×50 µm. Qualitative beam damage observations were based on 2 – 4 repeated scans, with total scan times of 8 – 12 minutes and 10 – 15 minutes per location for Fe- and S-XANES measurements, respectively.

260

2.2 Identifying and correcting Fe-XANES beam damage

Fe-XANES measurements were made in fluorescence mode at APS during analysis sessions in 2018 and 2019. The APS 13-ID-E beamline can deliver a focused, unattenuated X-ray beam to the sample at the Fe K-edge energy with a photon flux exceeding 1×10^{12} photons/s. Fully focused beam sizes of ~1×2 µm are achievable, providing flux densities up to 5×10^{11} photons/s/µm². Cottrell et al. (2018) and Moussallam et al. (2019) show that beam damage during Fe-XANES analysis scales with delivered photon dose over the measurement duration. Therefore, for the analyses presented here, photon dose was minimized during Fe-XANES analyses as follows:

1) Photon flux was attenuated using high-purity aluminum foil filters in the beam path (6 sheets of foil, totaling 222 µm thick), which decreased the incident photon flux to ~3 – 5×10^9 photons/s, consistent with an approach used in previous studies (Brounce et al., 2017; Moussallam et al., 2019; Tassara et al., 2020; Gaborieau et al., 2020).

2) Flux density on the sample was further decreased by defocusing the incident X-ray beam so that photon densities were generally 1 – 1.5×10^8, 2 – 4×10^7, and 6 – 9×10^6 photons/s/µm² for 5×5, 10×10, and 20×20 µm beam footprints, respectively.

3) Analysis times were minimized as much as possible while still providing interpretable spectra, which allowed us to reduce beam exposure.

The 13-ID-E monochromator calibration provides a first derivative of the Fe K-edge peak of iron foil at ~7110.7 eV, consistent with values determined by Kraft et al. (1996). We followed the Fe-XANES measurement methodology outlined in Head et al. (2018), but with modified scan times and energy ranges used to further identify and correct for beam damage. Two different analytical setups were used: rapid pre-edge scans and slower full energy scans. For rapid scans, the incident beam was scanned from 7092 – 7107 eV in 2.5 eV steps, from 7107 – 7119 eV in

285   0.1 eV steps, and from 7119 – 7144 eV in 0.05 Å^{-1} (0.5 – 1.0 eV) steps (continuous steps rather

286   than discrete). Each scan step was 0.5 seconds (s) and the total scan time was 82 s, with ~10 s

287   delay prior to the next analysis for beamline adjustment and computational processing. The rapid

288   pre-edge scans quickly measure over a reduced energy range to minimize beam exposure to the

289   extent possible while still collecting spectra with high enough resolution for peak fitting in the

290   pre-edge region. The 82 s scan is much faster than typical Fe-XANES scan durations reported in

291   the literature, which usually range from 270 s to >700 s (4.5 to >10 minutes) (e.g., Cottrell et al.,

292   2009, 2018; Moussallam et al., 2016; Head et al., 2018; Gaborieau et al., 2020; Tassara et al.,

293   2020). The slower, full energy range scans measured from 7012 – 7102 eV in 2.5 eV steps, from

294   7102 – 7120 eV in 0.1 eV steps, and from 7120 – 7356 eV in 0.05 Å^{-1} (0.5 – 3.0 eV) steps. Each

295   scan step time was either 0.5 or 1 s and total scan durations were 176 or 352 s. This full energy

296   range scan served as a higher-resolution scan of both the pre- and post-absorption edge regions,

297   which is similar to analytical procedures reported in other Fe-XANES studies and allowed

298   spectra to be normalized and assessed for mineral contamination.

299   Measured spectra were normalized to the incident flux ($K\alpha$ fluorescent intensity / incident

300   flux [I0]) and were fit using XAS viewer within the LARCH software package (Newville, 2013).

301    $Fe^{3+}/\Sigma Fe$ was calculated using relative pre-edge peak intensities following approaches described

302   in Cottrell et al. (2009). This approach uses the calculated centroid energy of the pre-edge

303   doublet, which is related to the 1s → 3d electron transition, to determine glass $Fe^{3+}/\Sigma Fe$ based on

304   calibrations to standard glasses equilibrated at known fO$_2$ conditions and measured using

305   Mössbauer spectroscopy (Berry et al., 2003; Wilke et al., 2004; Cottrell et al., 2009). An energy

306   offset between our basaltic glass measurements and those used in the Fe-XANES calibration of

307   Cottrell et al. (2009) (due to monochromator calibrations and background subtractions during

308   peak fitting) was determined by comparing the Fe pre-edge centroid position of basaltic

309   reference glass LW_0 (Cottrell et al., 2009, 2018; Zhang et al., 2016, 2018) from the

310   Smithsonian Institution. The split of LW_0 glass analyzed here is embedded in the mount

311   NMNH 118279/IGSN NHB007V34, and is the same specimen as found in the mount with

312   catalog number NMNH 117393/IGSN NHB0073V8 (both available by request from the

313   Smithsonian Institution). The pre-edge centroid position of LW_0 was measured by Cottrell et

314   al. (2009) to have an energy of 7112.30 eV using the beamline configuration they described at

315   the National Synchrotron Light Source (Brookhaven National Laboratory). All Fe-XANES

12

316   spectra in figures and data tables throughout this manuscript are presented in energy units as-

317   measured at APS. However, when calculating iron valences in basaltic glasses, energy shifts of

318   +0.317 and +0.323 eV were respectively applied to iron pre-edge centroid positions for

319   measurement sessions 2018-3 and 2019-2 to provide consistency with centroid values measured

320   for LW_0 in Cottrell et al. (2009). Pre-edge peak fitting ranges were similarly adjusted from

321   Cottrell et al. (2009) to span an energy range of 7108.7 – 7116.7 eV, consistent with the

322   methodology discussed in Zhang et al. (2016). Within this fit window, the absorption baseline of

323   the main Fe K absorption edge was fit using a linear and a Lorentzian function, and the pre-edge

324   doublet was fit using two Gaussian functions (Cottrell et al., 2009). The centroid value of the

325   these two peaks was used to calculate $Fe^{3+}/\Sigma Fe$ using the Mössbauer-based calibration of Zhang

326   et al. (2018) for basaltic glasses.

327   For dacitic and rhyolitic glasses, average iron valence was calculated from a

328   parameterization of Fiege et al. (2017) for felsic glasses. No energy offsets were applied because

329   our measurements of the first derivative of the absorption edge of iron foil were consistent with

330   those of Fiege et al. (2017). Uncertainties in centroid values (±1 SE), as detailed below, are

331   propagated through the basalt or rhyolitic calibrations to calculate uncertainties of $Fe^{3+}/\Sigma Fe$

332   calculations.

333

334   **2.2.1 Timescales of Fe-XANES beam damage**

335   Fe-XANES analysis of hydrous silicate glasses with a high intensity X-ray beam can

336   cause rapid photo-oxidation of Fe^{2+} to Fe^{3+} within the glass, creating large inaccuracies in

337   determining the initial $Fe^{3+}/\Sigma Fe$ values of glasses (Cottrell et al., 2018; Moussallam et al., 2019)

338   (Figure 2). The extent of this oxidation varies depending on glass composition and photon dose.

339   Beam-induced oxidation causes a shift in Fe-$K\alpha$ pre-edge peak intensities but does not produce

340   any uniquely identifiable spectral features. Consequently, it is impossible to know from a single

341   Fe-XANES analysis whether a sample had suffered from beam-induced photo-oxidation

342   (compare with S-XANES beam damage, which produced diagnostic spectral features, as

343   discussed in section 2.3). Therefore, samples must either be analyzed under carefully tested

344   analytical conditions to ensure that no significant beam damage occurs for the particular glass

345   composition and analysis duration, or a method must be employed that can identify and correct

346   for beam damage in each individual analysis spot. We emphasize the latter approach in this

347   study, presenting a method that allows us to reliably analyze small, hydrous glass inclusions with

348   a relatively high-flux beam.

349   To identify and correct for beam damage within each analysis spot, we conducted

350   multiple rapid scans of the Fe *K* pre-edge region to create a time series of progressive oxidation

351   (Figure 2). These time series allow us to assess whether beam damage occurred during analysis

352   and, if needed, enables us to calculate sample-specific corrections. For each analysis spot, we

353   conducted 3 to 6 rapid pre-edge scans (82 s) followed by one full energy scan (176 or 352 s)

354   across the entire Fe *K* absorption edge energy range. If pre-edge centroids calculated from the

355   rapid scans did not show progressive oxidation over time, the spectra were merged together to

356   form a single higher-resolution pre-edge spectrum. If changes in pre-edge centroid positions

357   were observed, we use the time series of centroid positions to extrapolate the centroid back to

358   t=0 s. We take this extrapolated value as the initial, 'correct' centroid position prior to beam

359   exposure. This time-dependent correction approach is similar to methods commonly applied to

360   electron microprobe measurements to account for alkali migration during electron beam

361   excitement (Kuehn et al., 2011). A time-dependent approach has also been recently proposed for

362   determining iron valence by electron microprobe measurements (Hughes et al., 2018).

363
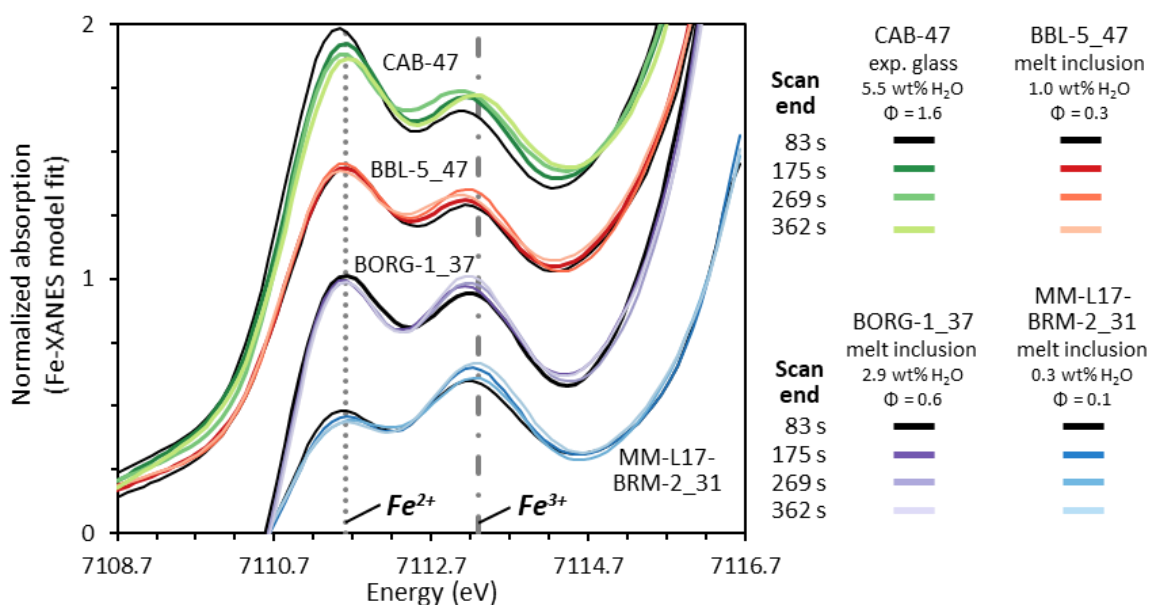
Figure 2. Model fits to Fe-XANES pre-edge spectra for repeated rapid scans of experimental
basaltic glass CAB-47 and of melt inclusions from the southern Cascades (CA, USA). Spectra of
different samples have been vertically shifted for clarity. Progressive oxidation occurs during
repeated rapid scans, as evidenced by the lighter colored lines. Samples have different initial

369 $Fe^{3+}/\Sigma Fe$ and H_2O contents, which affect the extent of beam-induced photo-oxidation.
370 Measurements were made with a 10×10 μm beam and photon flux densities ranged from $2 -$
371 4×10^7 photons/s/μm^2. The lines labeled Fe^{2+} and Fe^{3+} refer to the approximate positions of the
372 first and second pre-edge doublet peaks.
373

374   X-ray induced photo-oxidation during Fe-XANES analysis can be difficult to identify,

375 partly because a large extent of the valence change occurs rapidly in the first minutes of analysis

376 (Cottrell et al., 2018; Moussallam et al., 2019). To ensure that our sequences of repeated rapid

377 scans adequately captured changes to centroid positions during the earliest stages of photo-

378 oxidation, we measured changes to the intensity of the 2nd pre-edge doublet (at ~7113.4 eV at

379 APS) in single spots over $6 - 16$ minutes. Such dwell tests measure the photo-oxidation of the

380 analyzed glass at a much finer temporal resolution than pre-edge scans allow (Shorttle et al.,

381 2015; Cottrell et al., 2018; Moussallam et al., 2019; Gaborieau et al., 2020). However, one

382 limitation to such single-energy dwell tests are that other simultaneously changing spectral

383 features cannot be detected. Additionally, one must assume that any changes in spectral

384 background during the measurement duration are negligible.

385   We conducted a set of dwell tests on an experimental basaltic glass (CAB-47, Weaver et

386 al. [2011]) (Figure 3A, B) with a high H_2O content (5.5 wt%) and a high proportion of Fe^{2+}

387 (~0.13 $Fe^{3+}/\Sigma Fe$). Sample CAB-47 shows larger degrees of beam-induced oxidation of iron

388 compared to the natural glasses studied here, likely due to its combined high H_2O and Fe^{2+}

389 contents (Cottrell et al. 2018). The calculated beam damage susceptibility index (Φ, where $\Phi =$

390 $XHO_{0.5} * XFeO/XFeO_{1.5}$), as described in Cottrell et al. (2018), is 1.6 for CAB-47 compared to

391 Φ of $0.1 - 0.7$ for the various natural MI investigated in this study (Figure 5, Table 1). We

392 therefore use this highly beam damage-susceptible experimental glass to evaluate models for

393 correcting changing iron valence during Fe-XANES analysis.

394   To evaluate if time series of repeated rapid pre-edge scans (82 s durations, described

395 above) are sufficiently fast to capture photo-oxidation in CAB-47, we compared the pre-edge

396 rapid scan time series to the 2nd pre-edge doublet dwell tests in the same glass (Figure 3, Figure

397 A.1). It is assumed that the rate of change of the 2nd pre-edge doublet intensity scales with the

398 change in centroid value during time series analyses (Cottrell et al., 2018; Moussallam et al.,

399 2019). Dwell tests of the 2nd pre-edge doublet of CAB-47 with a photon flux density of ~1.4×10^8

400 photons/s/μm^2 (analyzed with a 5×5 μm spot size) show that substantial photo-oxidation occurs

401   in the first minute of analysis, with $Fe^{3+}/\Sigma Fe$ increasing from 0.13 to 0.19. Under these high

402   photon flux densities, photo-oxidation progresses non-linearly (Cottrell et al., 2018; Moussallam

403   et al., 2019; Figure 3, Figure A.1). The time series of repeated rapid pre-edge scans cannot

404   capture this non-linear behavior that occurs in the initial 10s of seconds of analysis, and therefore

405   cannot adequately characterize photo-oxidation at such high photon flux densities (Figure 3A,

406   C). However, by decreasing the photon flux density to $\sim 4.3 \times 10^7$ photons/s/μm^2 (using a 10×10

407   µm spot size), dwell tests of CAB-47 show that photo-oxidation is slow enough that changes to

408   both the 2nd pre-edge doublet intensity and centroid values can be adequately approximated by

409   fitting a linear function to repeated rapid pre-edge scans (Figure 3B, D). Although photo-

410   oxidation may remain non-linear in the initial minute of analysis even at this lower photon dose,

411   the linear fit approximates the data within typical measurement uncertainty and is thus a

412   reasonable approximation. The progression of photo-oxidation becomes more linear with further

413   decreased photon flux densities (Figure A.1).

414

415
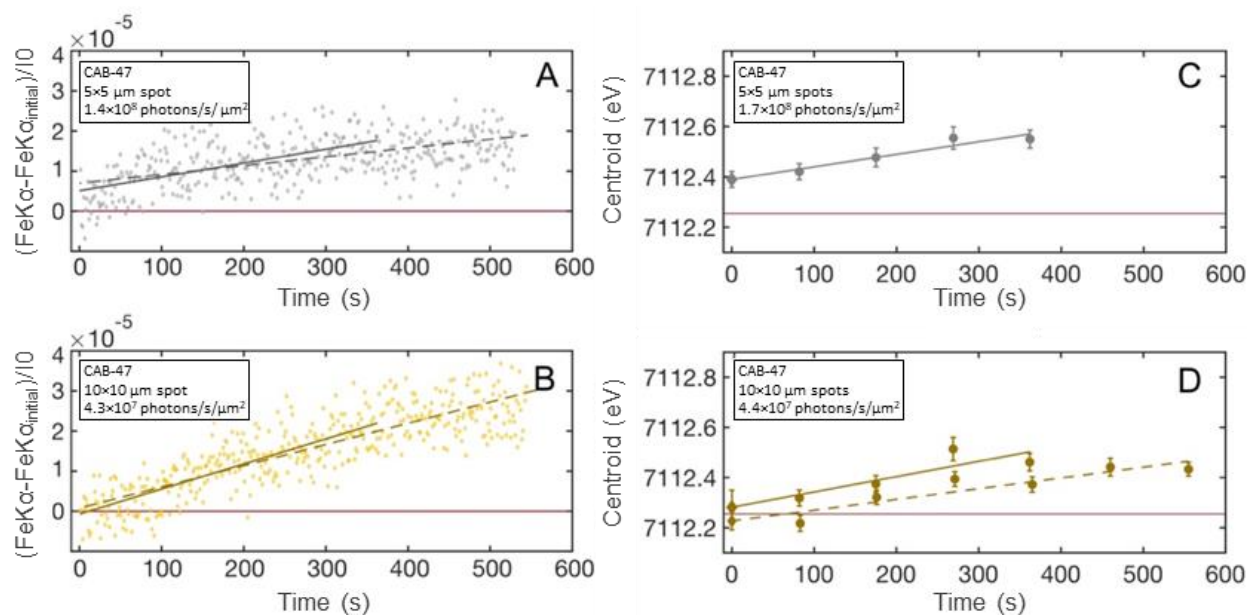
Figure 3. *(A, B)* Intensities of the 2nd pre-edge doublet as a function of time in experimental
glass CAB-47 measured with photon flux densities of 1.4×10^8 and 4.3×10^7 photons/s/μm^2 (5×5
µm and 10×10 µm respective spot sizes). Gray and yellow lines are linear regressions through
data from 0 to 362 s (solid) or 0 to 537 s (dashed). Fe-$K\alpha$/I0 initial intensity (red horizontal line)
is taken as the average of the first 5 analyses. *(C, D)* Pre-edge centroid positions calculated from
repeated rapid scans (see Figure 2) for experimental glass CAB-47 with photon flux densities of
1.7×10^8 photons/s/μm^2 (5×5 µm spot size; one time series) and $\sim 4.4 \times 10^7$ photons/s/μm^2 (10×10
µm spot size; two time series). Each circle is a centroid value calculated from one pre-edge scan

16

424   with error bars representing ±1 SE of centroid fits to each scan. Diamonds at t=0 s are the

425   intercept of linear regressions to each time series and are taken to be beam damage corrected

426   centroid values. Error bars on the t=0 s centroid positions represent ±1 SE of the time series

427   linear regression. Red lines in panels *C* and *D* are the estimated initial centroid value, which is

428   taken as the average beam damage corrected centroid values for the two 10×10 μm analysis time

429   series (panel *D*). Gray and yellow lines are linear regressions through centroid values from 82 to

430   362 s (solid) or 82 to 537 s (dashed). Centroid values in *C* and *D* have been shifted by +0.32 eV

431   for consistency with the LW_0 centroid position reported by Cottrell et al. (2009).

432

433   The same dwell tests were conducted using similar photon densities on another

434   experimental hydrous basaltic glass (CAB-33, 7.2 wt% H_2O, Φ = 1.8; Weaver et al., 2011) and

435   on a moderately hydrous natural obsidian pyroclast from Mono-Inyo Craters (CA, USA) (P2-F,

436   ~2.2 wt% H_2O; Barnes et al., 2014; Watkins et al., 2017; Table 1) Observed changes to the 2nd

437   pre-edge doublet intensity in these glasses were similar to those measured in CAB-47 (Figure

438   A.1), suggesting that the time series correction approach can be applied across a range of basalt

439   to rhyolite glass compositions, including hydrous samples that are highly susceptible to photo-

440   oxidation.

441

2.2.2 Applying the Fe-XANES beam damage correction technique to natural melt

inclusions

444   Because glass CAB-47 is more susceptible to beam damage than most MI and matrix

445   glasses, changes to pre-edge centroids in most natural samples analyzed under the same

446   conditions (~3.0×10^7 photons/s/μm^2) can also be approximated with a linear function. Hydrous

447   basaltic MI from the southern Cascades arc (0.3 – 3.7 wt% H_2O, Φ = 0.1 – 0.7) show consistent

448   increases in pre-edge centroid values over the course of several repeated rapid scans, indicating

449   progressive photo-oxidation (Figure 4, Table 1). In contrast, basaltic MI from Kīlauea Volcano

450   (HI, USA) do not show time-dependent changes to pre-edge centroid values, as expected based

451   on their low H_2O contents and low beam damage susceptibilities (0.1 – 0.3 wt% H_2O, $\Phi \leq$0.1)

452   (Figure 4, Table 1). The slopes of linear regressions to centroid time series (i.e., the rate of

453   photo-oxidation) are inversely correlated with calculated initial $Fe^{3+}/\Sigma Fe$ and are positively

454   correlated with H_2O contents of each glass (Figure 5, Figure A.2). These observations are

455   consistent with the findings of Cottrell et al. (2018) that beam damage occurs more readily in

456   reduced and/or hydrous glasses.

457   To apply time series corrections in beam damage-susceptible samples, linear regressions

458   using 4 rapid pre-edge scans are generally sufficient to correct to initial (t=0 s) centroid

459   positions. However, using up to 6 pre-edge scans can provide an improved regression fit, as

460   increased scans minimize the leverage of anomalously noisy scans in the regression (Figure 3D).

461   Uncertainties in restored initial centroid positions were assessed by calculating the standard error

462   of regression for each time series and by calculating the standard deviation of time series linear

463   fits using a Monte Carlo method that incorporates the standard error of each individual centroid

464   fit (Browaeys, 2021). For the analytical conditions used in this study, these two approaches yield

465   similar uncertainty estimates for the t=0 s centroid positions (Figure A.3). Weighting the linear

466   regressions by the inverse of the squared standard deviation of each measurement's uncertainty

467   also yields similar linear fits and standard error estimates for t=0 s centroid values. In time series

468   with substantial scatter in centroid positions, the standard error of linear regressions is generally

469   larger than the Monte Carlo-derived uncertainty estimates (Figure A.3). We therefore use the

470   standard error of unweighted linear regressions to estimate uncertainties in the restored t=0 s

471   centroid positions, as this is the simplest and generally most conservative approach.

472
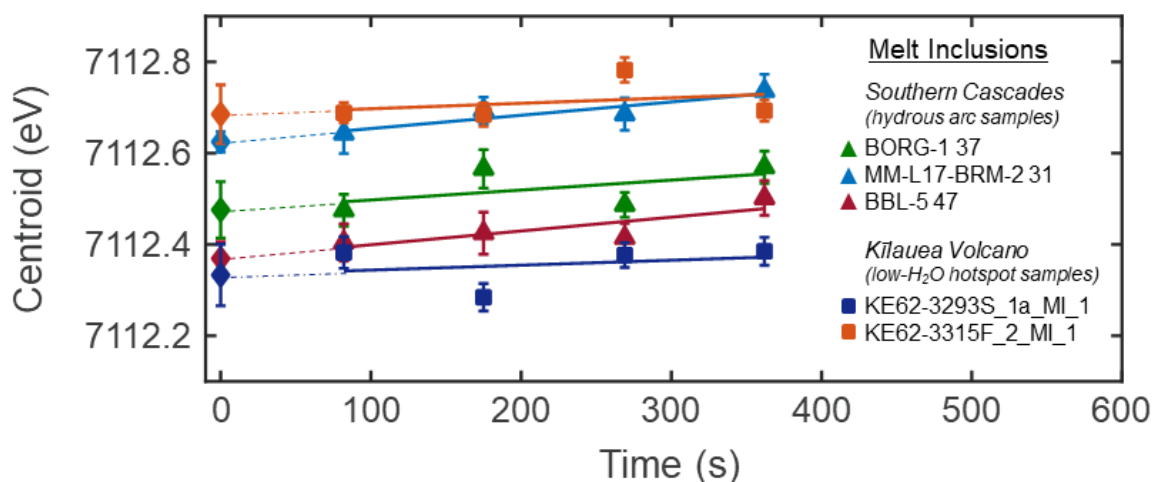
473

474   **Figure 4.** Fe *Kα* pre-edge centroid positions calculated from repeated rapid scans of MI from the

475   southern Cascades (triangles) and from Kīlauea Volcano (squares). Symbols are the centroid

476   values calculated from individual pre-edge scans and error bars represent ±1 SE for each centroid

477   fit. Lines are linear regressions through centroid values from 82 to 362 s. Diamonds at t=0 s are

478   the intercept of each regression (dashed lines), taken to be the beam damage corrected centroid

479   position. Error bars on diamonds represent ±1 SE of the time series linear regression. Analyses

480   used a 10×10 μm spot size, which resulted in photon flux densities of $3 - 5 \times 10^7$ photons/s/μm^2.

481   All centroids have been shifted by +0.32 eV for consistency with the LW_0 centroid position

482   reported by Cottrell et al. (2009).
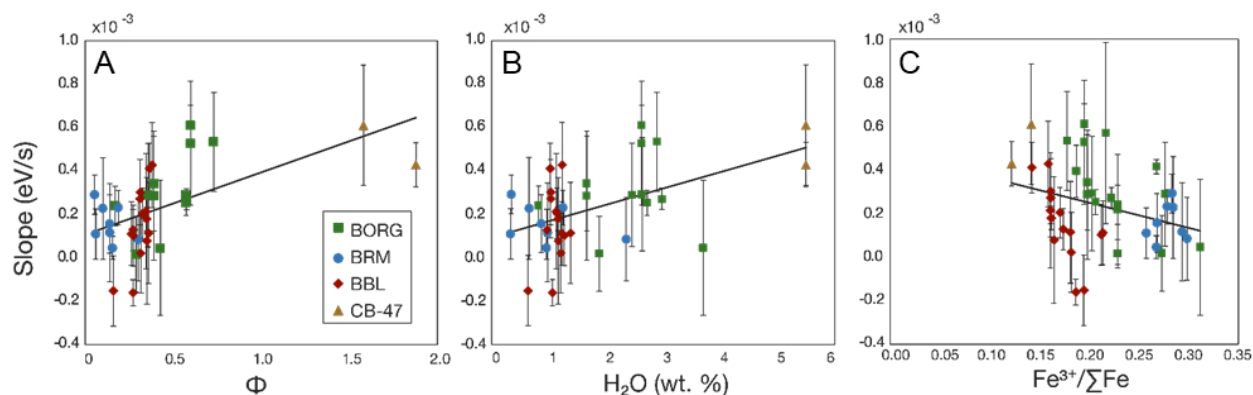
Figure 5. Slopes of linear regressions through centroid value time series for individual glasses plotted as a function of *(A)* beam damage susceptibility index ($\Phi = XHO_{0.5} * XFeO/FeO_{1.5}$) as defined in Cottrell et al. (2018), *(B)* H_2O content, and *(C)* initial $Fe^{3+}/\Sigma Fe$. Melt inclusions from southern Cascades cinder cones (BORG, BRM, BBL) and experimental glass analyses (CAB-47) are grouped by color. Gray lines are linear regressions through analysis spots from all natural and experimental samples.

For hydrous basaltic MI from the southern Cascades, the average 1 standard error of regression for corrected t=0 s centroid values is ±0.04 eV, or ±0.02 $Fe^{3+}/\Sigma Fe$ when propagated through the calibration of Zhang et al. (2018) (note that curvature of the calibration function increases $Fe^{3+}/\Sigma Fe$ uncertainties in more oxidized glasses). This uncertainty is only slightly larger than the average standard error of centroid value fits of our higher resolution full length scans (±0.03 eV; ±0.01 $Fe^{3+}/\Sigma Fe$), and is much smaller than the ~0.15 variation in $Fe^{3+}/\Sigma Fe$ measured in basaltic arc MI globally (Kelley and Cottrell, 2009; Brounce et al., 2014; Muth and Wallace, 2021). Regressions on replicate analyses within the same MI yield corrected centroid positions that are within error of each other (Figure A.4), indicating that our correction approach is reasonably accurate.

2.2.3 Discussion and summary

Although the time-dependent beam damage correction approach introduces some imprecision, it ensures that data sets are not systematically biased to higher calculated $Fe^{3+}/\Sigma Fe$ values due to uncorrected photo-oxidation. In analyses of basaltic MI from the southern Cascades (measured with photon flux densities of $1 - 5 \times 10^7$ photons/μm/s^2), the difference between corrected and uncorrected centroid positions is large (Figure 6). On average, centroid values measured after 362 s of analysis are 0.09 eV higher than t=0 s corrected centroid values.

19

509   This means that despite measures taken to lower the photon flux, had we analyzed these hydrous

510   MI with more typical 10-minute duration scans (where the pre-edge region is measured within

511   the first ~6 minutes) our analyses would have overestimated melt $Fe^{3+}/\Sigma Fe$ by ~0.036. This

512   would correspond to an overestimation of the fO_2 by 0.5 log units for basalt at 1150 °C and 400

513   MPa, according to the model of Kress and Carmichael (1991).

514

515
516
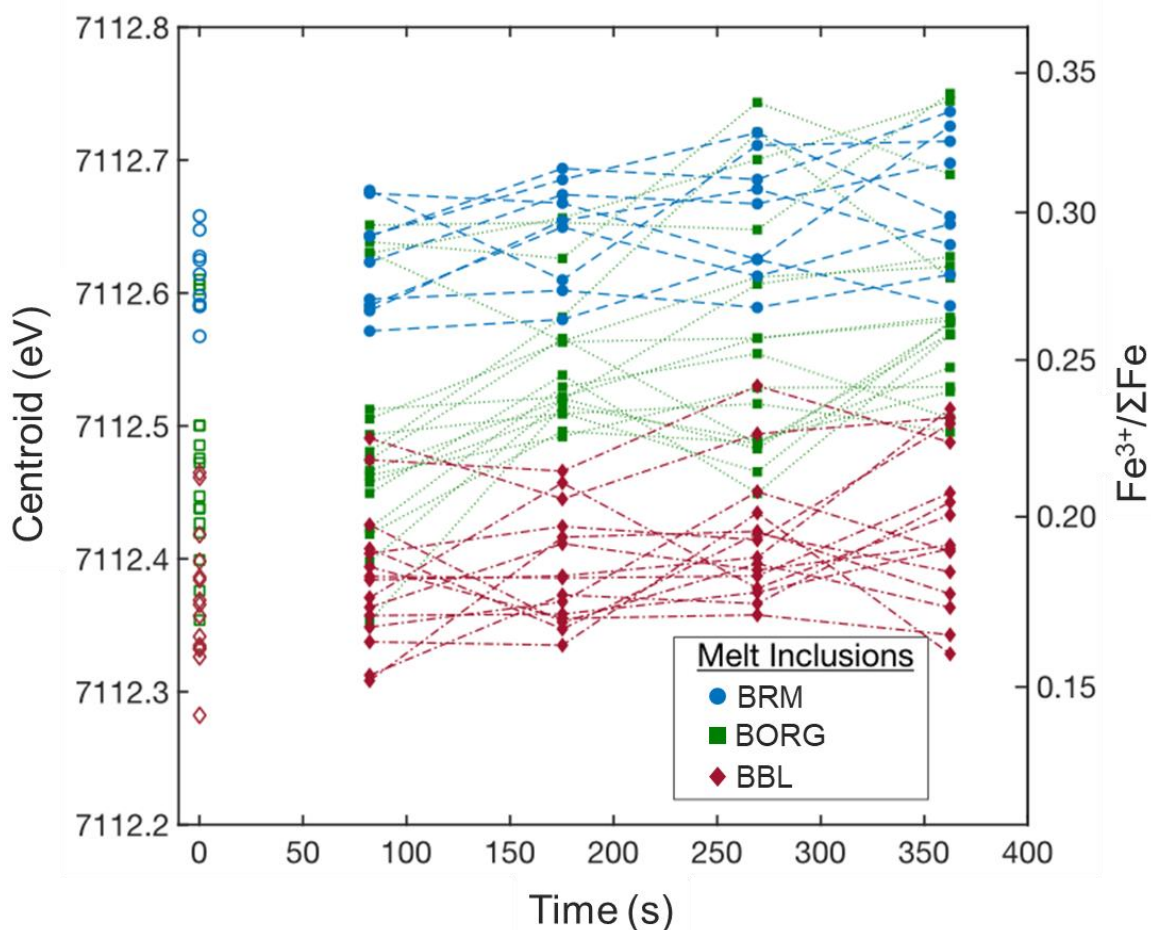
517
518   **Figure 6.** Fe-$K\alpha$ pre-edge centroid positions through time calculated from repeated pre-edge
519   scans for individual southern Cascades MI. Dashed lines connect centroids calculated from four
520   consecutive rapid scans of the same analysis spot, and open symbols at t=0 s are the corrected
521   initial centroids. Centroid time series measurements are plotted at the end time of each scan.
522   Right vertical axis is the calculated $Fe^{3+}/\Sigma Fe$ from centroid values using the calibration of Zhang
523   et al. (2018). All centroids have been shifted by +0.32 eV for consistency with the LW_0
524   centroid position reported by Cottrell et al. (2009).
525

526   In summary, photo-oxidation during Fe-XANES measurements can cause large

527   systematic biases toward higher calculated $Fe^{3+}/\Sigma Fe$ in beam-sensitive glasses, which can

528   significantly affect geologic interpretations of redox conditions (Cottrell et al., 2018;

529   Moussallam et al., 2019). Taking measures to mitigate beam damage through reduced X-ray flux

530   density (where possible) and/or by applying analysis-specific time-dependent corrections

531   described here is critical for accurate interpretation of Fe-XANES measurements in beam-

532   sensitive glasses, such as hydrous arc basalts. We present a time-dependent correction method

533   and set of analysis conditions that should enable beam damage identification and correction in

534   most natural silicate glasses at even relatively high photon flux densities ($10^7 - 10^8$

535   photons/s/μm^2). However, photo-oxidation during analysis is a function of glass composition

536   (including H_2O content and initial $Fe^{3+}/\Sigma Fe$), photon flux density, and duration of analysis, and

537   therefore depends on the specific sample and beamline properties. Best practices during Fe-

538   XANES analysis of glasses would include explicitly testing (via 2nd pre-edge multiplet dwell

539   tests) whether repeated rapid pre-edge scans sufficiently correct photo-oxidation for the

540   particular beamline conditions and sample composition being analyzed.

541

542   2.3 Identifying and correcting S-XANES beam damage

543   S-XANES measurements use lower X-ray energies than Fe-XANES (~2480 eV vs ~7110

544   eV, respectively) and therefore have smaller absorption lengths than Fe-XANES measurements.

545   At S-XANES energies, 95% of X-ray energy is absorbed within the upper ~15 μm of glass

546   (Wilke et al., 2011) (Figure 1A). The MI analyzed here are thicker than 15 μm so that doubly

547   intersecting the inclusions was not necessary for S-XANES analyses. Additionally, most host

548   minerals contain negligible sulfur compared to MI (Callegaro et al., 2020) so that beam overlap

549   of the host mineral is less of a concern than for Fe-XANES analyses, where iron signal

550   contribution from the host phase can be significant. Consequently, larger X-ray analysis

551   footprints can generally be used for S-XANES, which reduces X-ray dose and thereby

552   ameliorates some of the beam damage potential. However, when analyzing sulfur-poor MI

553   (<~400 ppm S), even slight contributions from the host phase might be significant relative to the

554   low-sulfur glass signal, and beam overlap of the host phase should be avoided. Additionally,

555   cracks and surface contaminants (e.g., oils) may be present on prepared surfaces, both of which

556   can contain undesired sulfur-bearing material (Brounce et al., 2019). Consequently, smaller

557   beam footprints for S-XANES remain more versatile for analysis of MI (particularly for low-

558   sulfur samples) because of the ability to avoid contamination from host minerals or from surface

559   aberrations.

560   Sulfur in silicate melts occurs as S^{2-} (sulfide complexes) or S^{6+} (sulfate complexes;

561    $S^{(VI+)}O_4^{2-}$) but does not naturally occur as S^{4+} (sulfite complexes; $S^{(IV+)}O_3^{2-}$) at the limit of

562   detection by XANES (Backnaes et al., 2008; Wilke et al., 2008, 2011). The main absorption

563   peak of S^{2-} complexes in glasses occurs over a broad energy range centered at ~2476 eV, and the

564   absorption peak of S^{6+} complexes occurs at ~2482 eV (Li et al., 1995; Paris et al., 2001; Bonnin-

565   Mosbah et al., 2002; Wilke et al., 2008; Métrich et al., 2009; Jugo et al., 2010). In Fe-bearing

566   natural glasses, S-XANES beam damage typically manifests as photo-reduction of S^{6+} to S^{4+}

567   (Wilke et al., 2008). The absorption peak for sulfite occurs at 2477.5 eV (note that the rapid

568   oxidation of sulfite at the surface causes a 2482 eV sulfate peak to also be present in the spectra

569   of most sulfite reference materials) (Métrich et al., 2002, 2009; Bonnin-Mosbah et al., 2002;

570   Fleet et al., 2005; Wilke et al., 2008; Jugo et al., 2010). The 2477.5 eV sulfite peak is a unique

571   spectral signal to recognize S^{4+} speciation and thereby can be used to identify measurements that

572   have undergone beam damage (Wilke et al., 2008; Métrich et al., 2009; Moussallam et al., 2014).

573   Beam damage is therefore more easily detected in S-XANES than in Fe-XANES, and time-

574   dependent corrections to t=0 s are not necessary because all observed S^{4+} is generally attributable

575   to beam-induced reduction of sulfur. Photo-reduction of S^{6+} has also been observed during

576   electron microprobe (EPMA) S-*K*α wavelength scans (Wilke et al., 2008). However, photo-

577   oxidation of S^{2-} to S^{4+} or to S^{6+} has been documented by other EPMA studies (Wallace and

578   Carmichael, 1994; Rowe et al., 2007) and during extremely long duration XANES measurements

579   (20 – 80 minutes) of highly alkalic glasses from Mt. Erebus (Antarctica) (Moussallam et al.,

580   2014). The predominance of sulfur photo-reduction during XANES analyses of natural glasses

581   suggests that different mechanisms of sulfur beam damage may occur under electron

582   bombardment compared to X-ray irradiation, and potentially also during X-ray irradiation of

583   alkali-rich glasses (Hughes et al., 2020).

584   The parameters influencing photo-reduction (S^{6+} to S^{4+}) in silicate glasses during S-

585   XANES irradiation are imprecisely known. In contrast to Fe-XANES beam damage (Cottrell et

586   al., 2018), H_2O content does not appear to be a critical control on S-XANES beam damage (see

587 section **2.3.3**), and the compositional dependence of S-XANES beam damage susceptibility has

588 not been thoroughly examined. It is consequently difficult to currently predict whether any

589 particular sample will be susceptible to S-XANES beam damage. Therefore, as with iron beam

590 damage, it is important to be able to account for beam damage within each individual

591 measurement rather than applying generalized corrections to an entire sample suite.

592   Our approach in managing and correcting S-XANES beam damage is similar to that for

593 reducing Fe-XANES beam damage, namely minimizing pre-analysis X-ray irradiation,

594 decreasing photon dose as much as possible while maintaining sufficient signal, and using repeat

595 rapid scans to observe beam-induced changes in sulfur speciation. Where S-XANES photo-

596 reduction is observed, we correct affected spectra by calculating the peak area of the beam

597 damage-induced S^{4+} signal and restoring this to original S^{6+} intensity via a calibrated conversion

598 factor (details below).

599

600 **2.3.1 S-XANES analytical conditions**

601   S-XANES measurements at APS GSECARS beamline 13-ID-E were conducted in

602 fluorescence mode and within a He-environment to minimize atmospheric absorption of the X-

603 ray fluorescent signal. Incident beam flux ranged from ~$1 - 40 \times 10^9$ photons/s for S-XANES

604 analyses, which was purposely lowered from the maximum possible flux to reduce rates of beam

605 damage. Repeat measurements of sulfate within Scotch® tape during four analytical sessions

606 between 2017 – 2020 indicate a consistent S^{6+} peak position of 2481.8 eV. The sulfate peak

607 position in crystalline hauyne measured by Jugo et al. (2010) at the European Synchrotron

608 Radiation Facility's beamline ID21 is +1 eV relative to sulfate measurements at APS beamline

609 13-ID-E, due to differences in monochromator calibration (Head et al., 2018). Thus, all the Jugo

610 et al. (2010) values presented in figures and data tables have been shifted by -1 eV for

611 consistency.

612   As with our Fe-XANES beam damage correction approach, we conducted repeat rapid

613 scans to identify S-XANES beam damage and, if necessary, applied sample-specific corrections.

614 Sulfur *K*-edge spectra were collected by scanning the incident beam from 2437 – 2467 eV in 2.5

615 eV steps, from 2467 – 2487 eV in 0.1 eV steps, and from 2487 – 2622 eV in 1.5 eV steps. Short

616 analysis times of either 0.5 or 1.0 s per step bin were used (continuous steps rather than discrete)

617 for rapid scans with total durations of 154 or 308 s, respectively. Three repeat scans were

618   typically conducted for each analysis spot, with cumulative measurement times of ~8 – 15

619   minutes per location. If S^{4+} peak growth was identified during successive scans, only the first

620   scan was used to quantify sulfur speciation, as this scan would have undergone the least S^{6+} to

621   S^{4+} photo-reductive beam damage. If no S^{4+} peak ingrowth was observed, the repeat scans were

622   merged to improve signal quality.

623   In beam-damaged samples, S^{6+} to S^{4+} photo-reduction can be corrected by restoring the

624   S^{4+} 2477.5 eV peak intensity back to a S^{6+} signal. This correction requires knowing an

625   appropriate signal intensity scaling factor to restore a S^{4+} signal to the original S^{6+} intensity.

626   Konecke et al. (2017) and Nash et al. (2019) apply S-XANES beam damage corrections by

627   assuming a 1:1 intensity scaling between S^{4+} and S^{6+} peaks. However, in the absence of direct

628   evidence, the accuracy of this assumed 1:1 scaling relationship of fluorescent energy outputs is

629   uncertain. To determine how the loss of S^{6+} intensity relates to the growth of S^{4+}, and therefore

630   how to calculate an appropriate signal intensity scaling factor between these peak intensities, we

631   conducted a series of measurements on a hydrous, sulfate-dominated, sulfur-rich experimental

632   basaltic glasses from Chowdury and Dasgupta (2019) (Table 1). The large area of this

633   experimental glass allowed a series of measurements with multiple spot sizes (2×2, 10×10,

634   20×20, and 50×50 μm) to observe varying degrees of beam damage under photon densities

635   ranging from $6.9×10^6 – 1.1×10^{10}$ photons/s/μm². The sulfate-only initial composition of this

636   oxidized glass made the identification of S^{4+} peak ingrowth obvious. With repeat measurements,

637   we are able to track the ingrowth of the S^{4+} 2477.5 eV peak (hereafter the "S^{4+} peak") at the

638   expense of the S^{6+} 2481.3 – 2482 eV peak. We can thereby quantify how the S^{4+} peak intensity

639   relates to the loss of S^{6+} intensity, and how consistent the S^{4+} to S^{6+} intensity scaling relationship

640   is with increasing degrees of beam damage.

641

2.3.2 Quantifying S-XANES spectra via peak fitting

643   Determining the relationship between S^{4+} signal growth and S^{6+} signal loss during S-

644   XANES beam damage requires a consistent peak fitting method to quantify the change in

645   absorption intensities. Peak fitting approaches to S-XANES spectra have been employed by

646   other researchers (Manceau and Nagy, 2012; Konecke et al., 2017; Nash et al., 2019), but have

647   not been described or calibrated in silicate glasses at the level of detail required to be fully

648   reproducible. We therefore establish a new peak fitting calibration based on the dataset used by

649   Jugo et al. (2010) to originally define a calibration relating S-XANES signal intensities to sulfur

650   speciation. S-XANES spectra of silicate glasses are produced by a mixture of X-ray photon

651   absorptions by S^{2-}, S^{4+}, and S^{6+} species, and by S^{1-} and S^{2-} sulfide complexes (Paris et al., 2001;

652   Fleet et al., 2005; Métrich et al., 2009). Jugo et al. (2010) empirically determined a relationship

653   of S^{2-} and S^{6+} X-ray absorption intensities to sulfur speciation using a set of experimental glasses

654   by integrating all signal within energy ranges relating to S^{2-} and S^{6+} peaks (2474.7 – 2479 eV and

655   2480.5 – 2483 eV, respectively; Jugo et al. [2010] ranges have been shifted by -1 eV). However,

656   the S^{4+} absorption peak (2476.8 – 2477.6 eV) occurs within the broad S^{2-} energy range.

657   Consequently, the Jugo et al. (2010) approach would inappropriately include any photo-

658   reduction induced S^{4+} signal intensity as S^{2-} intensity. Our peak fitting approach differentiates S^{2-}

659   , S^{4+}, and S^{6+} absorption intensities, enabling us to quantify beam damage by isolating S^{4+} from

660   the S^{2-} peak. We can then restore the S^{4+} photo-reduction signal to an original S^{6+} intensity to

661   calculate the undamaged sulfur speciation of the glass.

662   Our S-XANES peak fitting method again uses the spectral fitting program XAS viewer

663   (Newville, 2013) to correct for instrument deadtime and to fit the S-XANES data. Measured

664   spectra were first scaled by the Si-$K\alpha$ signal intensity, to avoid aberrations in incident beam

665   intensity over the analysis energy range due to possible contaminants within the beamline optics.

666   Following the approach of Jugo et al. (2010) and Anzures et al. (2020), we then normalize each

667   spectrum so that the energy range containing pre-edge features begins at zero intensity (~2467

668   eV), and the post-edge signal intensity is 1 (>2510 eV). This is done by defining a linear relation

669   in the low energy range (~2441 – 2467 eV), and flattening the high energy range (~2525 – 2611

670   eV) to scale the spectra to between 0 – 1 (Ravel and Newville, 2005; Anzures et al., 2020). These

671   energy ranges for normalization are guidelines that should be slightly modified as necessary if

672   anomalous data points are present for particular scans. However, sulfide X-ray absorption begin

673   at energies just above 2467, so the pre-edge normalization range should be kept below this

674   energy. The normalized post-edge spectrum is fit using an error function and a broad Gaussian,

675   which together define the background. The center point of the error function is fixed and the

676   width of the high-energy Gaussian is constrained to maintain a consistent background fitting

677   approach for all spectra (Table 2).

678   Assessing S-XANES spectra of >100 reduced and oxidized glass analyses across a

679   compositional range from basaltic to rhyolitic (Table 1; **Data supplement**), we identify the

680   energy ranges of five peaks within the S-$K\alpha$ absorption region. We distinguish four absorption

681   peak ranges that have been recognized as corresponding to sulfide complexes, and S^{2-}, S^{4+}, and

682   S^{6+} species (Wilke et al., 2008, 2011; Métrich et al., 2009; Jugo et al., 2010; Head et al., 2018)

683   (Table 2). We additionally identify an absorption peak between 2483.5 – 2486 eV, which is

684   slightly higher energy than the main S^{6+} peak. This 2483.5 – 2486 eV energy peak was similarly

685   identified by Konecke et al. (2017), who refer to it as the sulfur "ionization peak", a term we

686   adopt here. The sulfur-ionization peak intensity seems partially correlated to S^{6+} intensity, but is

687   also present in S^{2-}-dominated spectra. After normalizing the spectra, we simultaneously fit the

688   background with an error function and Gaussian and fit five separate Gaussian functions for each

689   of the sulfur absorption features (Figure 7, Figure A.6). Table 2 provides the energy ranges and

690   peak width tolerances for fitting each spectral feature. These fitting ranges have been established

691   to provide flexibility in fitting slight differences in peak energies occurring across a range of

692   compositions and oxidation states, while maintaining peak positions that accurately correspond

693   to the specific sulfur features (important for overlapping features such as the S^{2-} and S^{4+} peaks,

694   and the S^{6+} and ionization peaks).

695

696   **Table 2.** Peak definitions and fit parameters used for quantification of normalized S-XANES
697   spectra intensities using the XAS Viewer spectral fitting program (Newville, 2013). See **Data**
698   **supplement** for example peak fit models.

S-XANES feature	function type / name	peak center bounds (eV)	peak sigma bounds (width)	peak amplitude bounds
overall fit ranges				
peak fit range	-	2455 – 2550	-	-
pre-edge fit range	-	2466 – 2487	-	-
background fitting				
baseline error function	error1	2485 (fixed)	8 (fixed)	0 – 1.1
baseline Gaussian	gauss1	2493 – 2500	0 – 10	0 – 15
Sulfur speciation peaks				
sulfide complexes	gauss2	2465 – 2470	0 – 1	0 – ∞
S^{2-} (sulfide in glass)	gauss3	2475.3 – 2477	2 – 4	0 – ∞
S^{4+} (sulfite)	gauss4	2476.8 – 2477.7	0.1 – 1	0 – ∞
S^{6+} (sulfate)	gauss5	2480 – 2482.3	0.1 – 3	0 – ∞
sulfur ionization peak	gauss6	2483.5 – 2486	0 – 4	0 – ∞

699

700   To relate the relative fitted peak areas to sulfur speciation, we calibrate our peak fitting

701   method to experimental hydrous basaltic glasses presented in Jugo et al. (2010). Following the

702   same approach as Jugo et al. (2010), we use their completely S^{2-}-bearing and completely S^{6+}-

703   bearing experimental glasses as reduced and oxidized end-members, and apply linear

704   combination fitting of these end-members to produce representative mixed speciation spectra

705   (Figure A.5). Complete details are provided in the **Supplementary information**.

706   Jugo et al. (2010) focus their S-XANES calibration on only S^{2-} and S^{6+} peak intensities,

707   and do not include signals from lower energy sulfide-complexes or higher energy features

708   beyond the S^{6+} peak. We follow this approach, and although we fit all spectral features in the

709   calibration glasses, we use only the S^{2-} and S^{6+} peak areas to quantify the sulfur speciation in

710   glasses (Figure 7, Figure A.6). Jugo et al. (2010) describe an exponential function to relate S^{2-}

711   and S^{6+} peak intensities to sulfur speciation, however we find that the following empirical

712   polynomial relationship is more appropriate for our peak fitting method (Figure A.7):

713   *$S^{6+}/\Sigma S = 0.1733 * (I[S^{6+}]/\Sigma I[S^T])^2 + 0.8343 * (I[S^{6+}]/\Sigma I[S^T])$, [Eq. 1]*

714   where *$S^{6+}/\Sigma S$* is the fraction of S^{6+} out of total sulfur in the glass, and *$I[S^{6+}]/\Sigma I[S^T]$* is the

715   XANES-measured S^{6+} intensity (Gaussian peak area) out of the combined total intensities of the

716   S^{6+} peak and the broad S^{2-} peak (*$I[S^{6+}]+ I[S^{2-}]=I[S^T]$*). This peak fitting approach accurately

717   reproduces observations from additional glasses synthesized by Jugo et al. (2010) across a range

718   of *f*O_2 and sulfur speciation (Figure A.8). We therefore conclude that our peak fitting approach is

719   similar to the calibration (and this compatible with the thermodynamic relations) originally

720   described by Jugo et al. (2010), while additionally allowing the quantification of a S^{4+} peak. We

721   note that our method is subject to the same limitations as the Jugo et al. (2010) approach,

722   namely, that the linear end-member mixing approach to calibrate mixed sulfur speciation melts is

723   valid. Additional uncertainty arises from inconsistencies with normalizing S-XANES spectra,

724   which can be challenging in sulfur-poor glasses. Unfortunately, raw S-XANES spectra are

725   seldom published, which precludes assessing consistency in normalization approaches between

726   studies. For reproducibility of spectral processing by future workers, it is important that both the

727   raw and the normalized/flattened S-XANES data be made available (see **Data supplement**)

728   (Rose-Koga et al., 2021).

729   The average precision of our S-XANES peak fitting method, based on multiple analyses

730   in single MI and within regions of mid-ocean ridge basalt (MORB) glasses, is ±7% relative (2

731   RSE, 19 analyses in glasses ranging from 0.07 to 0.85 $S^{6+}/\Sigma S$; see **Data supplement**). When

732   considering further uncertainties in the peak fitting calibration and from the non-uniqueness of

733   spectra normalization (particularly in signal-limited samples), we assume the total accuracy of

734   this method to be better than ±10% relative.

735
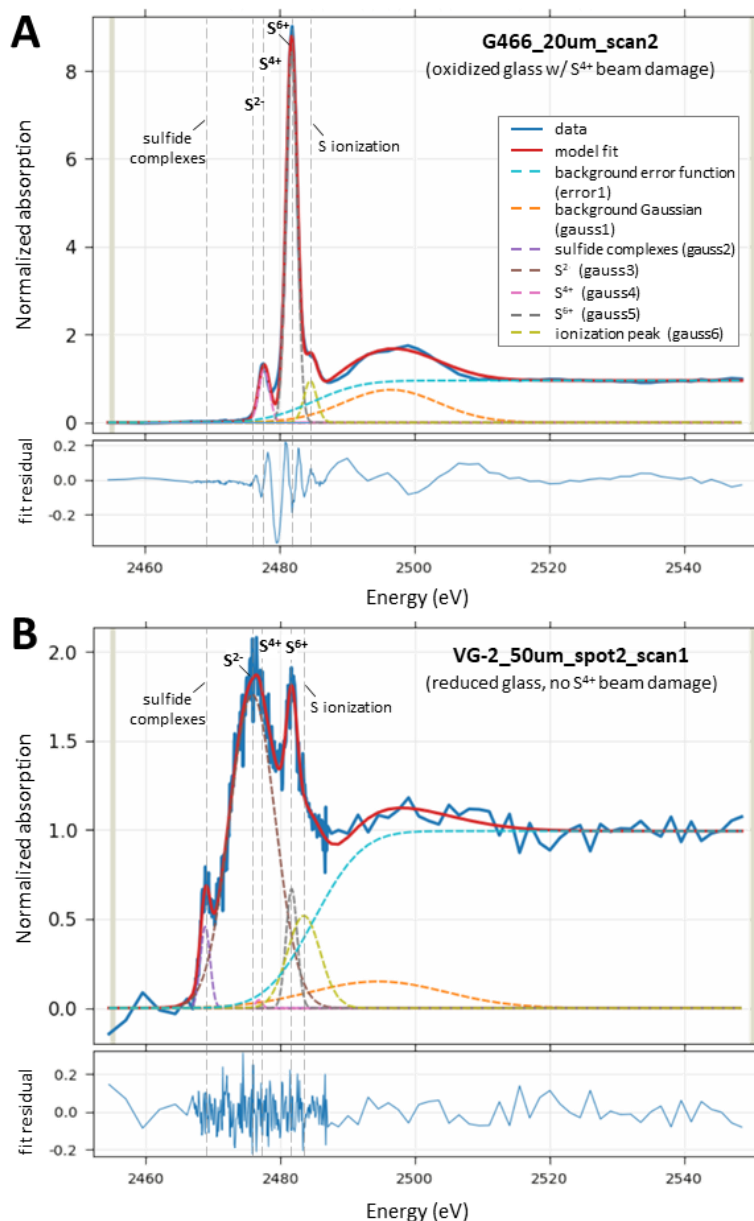
736

737   **Figure 7**. *(A)* Example S-XANES peak fitting to oxidized experimental glass G466. This

738   spectrum is the 2nd of 3 repeat scans with a 20×20 μm beam (photon flux density of $1.1×10^8$

739   photons/s/μm^2) and shows a dominant S^{6+} peak (2480 – 2482.3 eV) and a substantial beam

740   damage-induced S^{4+} peak (2476.8 – 2477.7 eV). No S^{2-} intensity is observed. The fit residual

741   shows slight remaining unfit structure. *(B)* Example S-XANES peak fitting of reduced VG-2

742   MORB glass analyzed using a 50×50 μm beam (photon flux density of 6.2×10^6 photons/s/μm^2).
743   The noisier spectrum is due to lower sulfur content in VG-2 than G466, as well as a difference in
744   vertical scale. A main glassy S^{2-} peak (2475.3 – 2477 eV) is present, as well as a lesser S^{6+} peak
745   and a minor sulfide peak (2465 – 2470 eV). Minimal S^{4+} beam damage ingrowth is observed
746   with this diffuse beam analysis (compare to Figure 9). A sulfur-ionization peak (2483.5 – 2486
747   eV) is present in S-XANES spectra of the both oxidized and reduced glasses. See Table 2 for
748   identification of peaks and fit parameters. Reference peak position lines may vary slightly
749   between samples depending on bond coordination environments.
750

2.3.3 Correcting S-XANES beam damage

752   Since we include the S^{4+} peak in our fitting methodology, we can quantitatively separate

753   the beam damage-induced S^{4+} signal from the overlapping broad S^{2-} peak in S-XANES spectra.

754   This was not possible with the Jugo et al. (2010) method because all signal intensity over this

755   region was considered as S^{2-}, which would lead to spurious results in beam-damaged spectra

756   (Figures 8, 9). During repeat measurements of hydrous, sulfur-rich, oxidized, anhydrite-saturated

757   experimental basaltic glasses G466 and G479 (50 – 51 wt% SiO$_2$, 9000 – 15000 ppm S, 6.5 – 8.9

758   wt% H$_2$O, 1300 – 1325 °C, 1.5 – 2.0 GPa; Table 1; Chowdhury and Dasgupta, 2019), we

759   observe that progressive irradiation leads to increasing S^{4+} intensity and concomitant decreasing

760   S^{6+} intensity (Figure 8) (Wilke et al., 2008; Métrich et al., 2009; Konecke et al., 2017). Because

761   these glasses are highly oxidized, they contain no S^{2-} signal to overlap with the S^{4+} peak, which

762   makes observation of the S^{4+} signal straightforward. As expected, increased photon doses with

763   more focused beams cause more rapid S^{6+} to S^{4+} photo-reduction. Comparing the intensity ratio

764   of S^{4+} peak ingrowth and S^{6+} peak loss during progressive beam damage from repeat

765   measurements with photon flux densities ranging from 10^6 to 10^{10} photons/s/μm^2, we find that

766   S^{4+} peak ingrowth relates to S^{6+} intensity decrease by a factor of 1.2 ± 0.1 (1 SE; n = 7) (see

767   **Data supplement**). We apply this scaling factor to observed S^{4+} peak intensities in beam

768   damaged samples to restore original S^{6+} peak intensities via:

769   $$\Sigma I[S^{6+}] = (I[S^{4+}] * F_S^{4+/6+}) + I[S^{6+}], \text{ [Eq. 2]}$$

770   where $\Sigma I[S^{6+}]$ is the restored total S^{6+} S-XANES intensity, $I[S^{4+}]$ and $I[S^{6+}]$ are the measured

771   Gaussian peak areas from S-XANES intensities, and $F_S^{4+/6+}$ is the S^{4+} to S^{6+} intensity scaling

772   factor (1.2 ± 0.1; though this may be compositionally dependent, as discussed below). The ratio

773   of S^{6+} signal intensity to total sulfur intensity is then:

774   $$I[S^{6+}] / \Sigma I[S^T] = \Sigma I[S^{6+}]/ (I[S^{2-}] + \Sigma I[S^{6+}]), \text{ [Eq. 3]}$$

775   Inputting this value into our peak fitting calibration based on the Jugo et al. (2010) glass suite

776   (Eq. 1) calculates the beam damage-restored sulfur speciation.

777   In addition to the obvious S^{4+} peak growth during beam damage of G466 and G479

778   glasses, we observe the ingrowth of a very small peak between 2471.6 – 2472.0 eV (Figure 8

779   inset), which is in the energy absorption range attributed to S^0 (Fleet et al., 2005; Métrich et al.,

780   2009) or H_2S (Klimm et al., 2012a). This 2471.6 – 2472.0 eV peak is recognized during

781   successive analyses using 2×2, 10×10, and 20×20 μm spots (10^{10} to 10^8 photons/s/μm^2), but is a

782   negligible feature compared to the S^{4+} and S^{6+} signals. We also observe a slight absorption

783   increase in the broad energy range between 2470 – 2475 eV, which overlaps the S^{2-} glassy

784   absorption range. These subtle features are not included in our beam damage correction

785   approach, as peak-fitting such low-intensity features was inconsistent and sensitive to slight

786   variations in the spectra normalization routine. However, these additional features of S-XANES

787   beam damage invite future investigation.

788

789
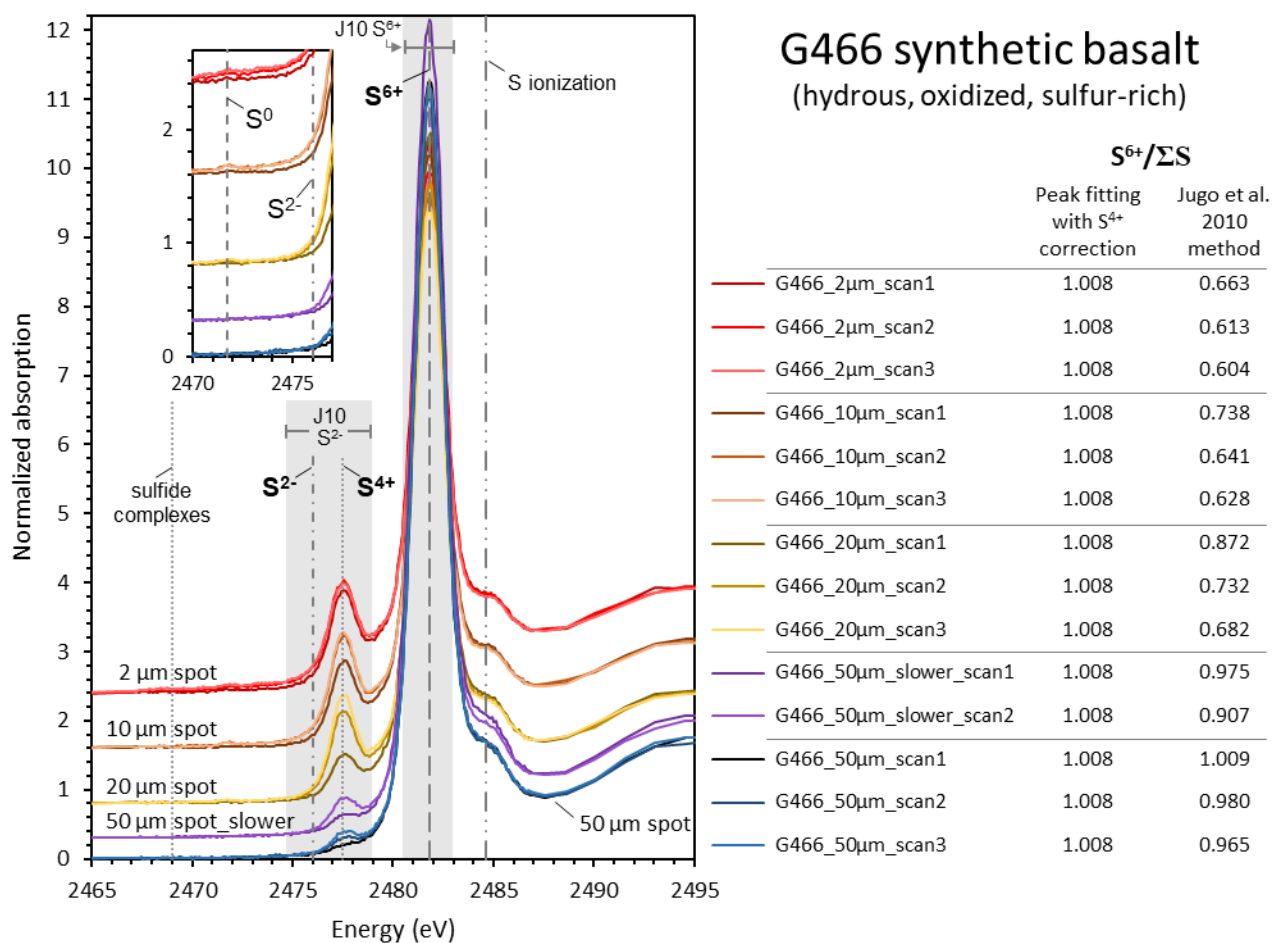
Figure 8. Normalized spectra of oxidized, anhydrite-saturated, experimental glass G466 with repeat measurements in different locations with progressively greater photon flux densities (6.2×10^6, 4.3×10^6, 1.1×10^8, 4.2×10^8, and 1.1×10^{10} photons/s/μm^2 for the 50μm, 50μm_slower, 20μm, 10μm, and 2μm scans, respectively). Spectra have been vertically shifted for clarity. The ingrowth of S^{4+} (2476.8 – 2477.7 eV) at the expense of S^{6+} (2480 – 2482.3 eV) is seen in repeat measurements at all spot sizes, and is increasingly pronounced with more focused beams. S^{4+} ingrowth stops after reaching a maximum intensity during the first focused 2×2 μm spot analysis, with no further ingrowth during subsequent analyses. *(inset)* Detailed view of the 2470 – 2476 eV region showing the ingrowth of a small peak at ~2471.7 eV and a slight absorption increase across 2470 – 2475 eV in analyses with focused beams. Each individual scan length was 5 minutes, except for G466_50um_scans that were each 10 minutes. $S^{6+}/\Sigma S$ calculations using the peak fitting approach and correcting for S^{4+} photo-reduction are compared with $S^{6+}/\Sigma S$ calculated using the Jugo et al. (2010) method ("J10" gray S^{2-} and S^{6+} regions [energy shifted as discussed]), where the S^{4+} photo-reduction peak would be counted as part of the S^{2-} signal. Reference peak position lines may vary slightly between samples.

807   **2.3.4 Observations of natural glasses and melt inclusions**

808   We observe the same rapid S^{6+} to S^{4+} photo-reduction in numerous natural glasses.

809   Hydrous basaltic MI from the southern Cascades (up to 3.7 wt% H_2O) undergo rapid photo-

810   reduction (Muth and Wallace, 2021), which is consistent with hydrous basalts being highly

811   susceptible to speciation changes during X-ray irradiation (Cottrell et al., 2018; Moussallam et

812   al., 2019). However, we also observe rapid photo-reduction during S-XANES analyses of low-

813   H_2O tholeiitic basaltic glasses that have been observed to be very stable during Fe-XANES

814   analyses (Cottrell et al., 2009; Zhang et al., 2018). Repeated rapid S-XANES scans of the MORB

815   glass standard VG-2 (NMNH 111240-52; Juan de Fuca ridge) again show a marked decrease in

816   S^{6+} and ingrowth of S^{4+} during successive analyses (Figure 9). S-XANES measurements of VG-2

817   have been presented elsewhere (e.g., Head et al., 2018), but have typically been analyzed with a

818   more focused beam and longer measurement times than used here, which we observe to cause a

819   near complete conversion of S^{6+} to S^{4+}. VG-2 glass is relatively reduced (0.15 $Fe^{3+}/\Sigma Fe$, fayalite-

820   magnetite-quartz buffer [FMQ] +0.0; Zhang et al., 2018) so that the original S^{6+} is low and the

821   photo-reduction S^{4+} peak is correspondingly small. The small S^{4+} peak is therefore difficult to

822   discern from the dominant S^{2-} peak, which potentially explains why beam damage in VG-2 glass

823   has not been previously recognized. A North Pacific MORB glass analyzed via S-XANES with a

824   defocused beam by Métrich et al. (2009) also had a recognizable small S^{6+} peak, consistent with

825   our observations of VG-2. Applying our peak fitting and S^{4+} to S^{6+} correction approach to the

826   least beam-damaged VG-2 analyses (50×50 μm spot size; 1.1×10^7 photons/s/μm^2 flux density),

827   we estimate that VG-2 MORB glass has 0.079 ± 0.003 $S^{6+}/\Sigma S$ (1 SE, n = 4). S-XANES

828   measurements of two additional MORB glasses, JDF-46N and ALV892-1 (Woods Hole

829   Oceanographic Institution, Northeast National Ion Microprobe Facility internal standards), at low

830   photon flux densities ($2 - 3\times10^7$ photons/s/μm^2) give similar $S^{6+}/\Sigma S$ of 0.081 ± 0.001 and 0.093

831   ± 0.001, respectively (1 SE, n=4 for each glass). Tests at higher photon flux densities ($10^8 - 10^{10}$

832   photons/s/μm^2) or with long analysis durations (>6 minutes) show that JDF-46N and ALV892-1

833   also undergo rapid S^{6+} to S^{4+} photo-reduction (Figure 10), indicating a common susceptibility for

834   X-ray induced photo-reduction among low-H_2O MORB samples.

835   The measured 0.08 – 0.09 $S^{6+}/\Sigma S$ in these three MORB samples are similar to the upper

836   end of the 0.03 – 0.07 $S^{6+}/\Sigma S$ range measured in MORB glasses via EPMA S-$K\alpha$ wavelength

837   shift (Wallace and Carmichael, 1994) (although the EPMA-measured samples may have suffered

838 from electron beam-induced photo-oxidation [Jugo et al., 2010]). These measurements are all

839 elevated compared to the 0.00 – 0.02 $S^{6+}/\Sigma S$ measured by S-XANES in four MORB glass

840 samples by Jugo et al. (2010). Based on global MORB average fO_2 estimates of FMQ -0.17 ±

841 0.15 (0.014 ± 0.01 $Fe^{3+}/\Sigma Fe$) by Cottrell et al. (2020) or FMQ +0.1 by Berry et al. (2018), the

842 Jugo et al. (2010) relationship of S^{6+} to fO_2 predicts that MORB glasses should contain almost

843 exclusively sulfide (≤0.01 $S^{6+}/\Sigma S$). However, our observations indicate that MORB glasses are

844 not universally sulfate-free and, at least in the three localities analyzed here, contain low but

845 resolvable S^{6+} (up to 0.09 $S^{6+}/\Sigma S$).

846

		Peak fitting w/ S^{4+} correction	Jugo et al. 2010 method
VG-2 2um_scan1		0.042	-0.030
VG-2 2um_scan2		0.031	-0.039
VG-2 10um_scan1		0.064	0.024
VG-2 10um_scan2		0.048	0.011
VG-2 10um_scan3		0.057	0.001
VG-2 20um_scan1		0.070	0.032
VG-2 20um_scan2		0.077	0.025
VG-2 20um_scan3		0.064	0.026
VG-2 50um spot2_scan1		0.076	0.055
VG-2 50um spot2_scan2		0.080	0.056
VG-2 50um spot2_scan3		0.072	0.057
VG-2 50um spot1_scan1		0.087	0.061
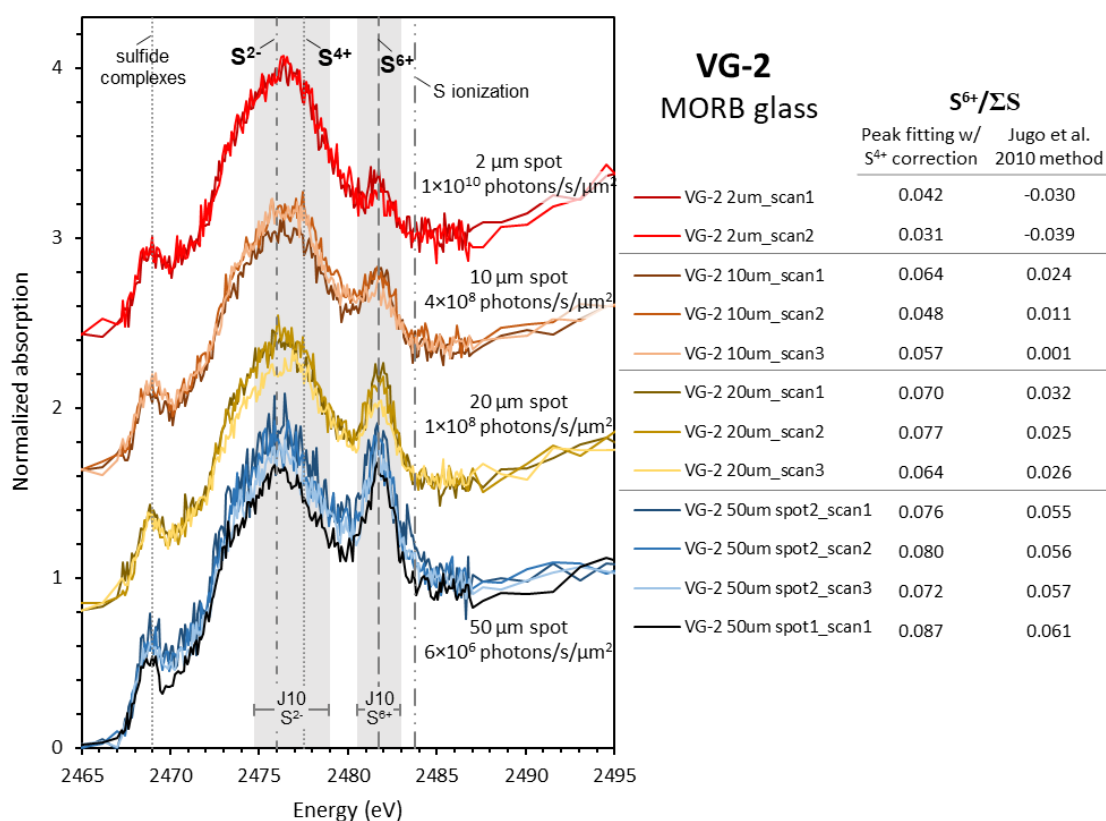
848 **Figure 9**. Normalized S-XANES spectra of MORB glass standard VG-2 with repeat
849 measurements in different locations using progressively greater photon flux densities (6.4×10⁶,
850 1.1×10⁸, 4.3×10⁸, 1.1×10¹⁰ photons/s/μm² for the 50μm, 20μm, 10μm, and 2μm scans,
851 respectively). Spectra have been vertically shifted for clarity. The ingrowth of S^{4+} (2476 –
852 2477.7 eV) and loss of S^{6+} (2480.5 – 2483.3 eV) is increasingly apparent during analysis with
853 more focused beams. Measurements with a fully focused 2×2 μm beam cause the S^{6+} signal to be
854 almost completely lost. Note the difficulty of recognizing the S^{4+} peak against the dominant S^{2-}
855 broad peak at 2472 – 2480 eV, giving the illusion of a beam damage-free spectra. Each
856 individual scan duration was 5 minutes. $S^{6+}/\Sigma S$ calculations using the peak fitting approach and
857 correcting for S^{4+} photo-reduction are compared with $S^{6+}/\Sigma S$ calculated using the Jugo et al.

858 (2010) method ("J10" gray S^{2-} and S^{6+} regions [energy shifted as discussed]), where the S^{4+}
859 photo-reduction peak would be counted as part of the S^{2-} signal. Reference peak position lines
860 may vary slightly between samples.
861

JDF-46N MORB glass

	Total analysis time (s)	$S^{6+}/\Sigma S$ Peak fitting with S^{4+} correction	Peak fitting w/ no S^{4+} correction
JDF-46N 2µm_scan1	304	0.062	0.055
JDF-46N 2µm_scan2	622	0.052	0.043
JDF-46N 2µm_scan5	1575	0.035	0.034
JDF-46N 2µm_scan10	3168	0.037	0.036
JDF-46N 2µm_scan20	6351	0.044	0.041
JDF-46N 20µm_scan1	304	0.082	0.082
JDF-46N 20µm_scan2	622	0.077	0.075
JDF-46N 20µm_scan5	1575	0.069	0.064
JDF-46N 20µm_scan10	3168	0.061	0.051
JDF-46N 20µm_scan20	6351	0.053	0.039
JDF-46N 50µm_scan1	304	0.084	0.084
JDF-46N 50µm_scan2	622	0.077	0.077
JDF-46N 50µm_scan5	1575	0.080	0.078
JDF-46N 50µm_scan10	3168	0.071	0.070
JDF-46N 50µm_scan20	6351	0.072	0.068

ALV892-1 MORB glass

	Total analysis time (s)	$S^{6+}/\Sigma S$ Peak fitting with S^{4+} correction	Peak fitting w/ no S^{4+} correction
ALV892-1 2µm_scan1	152	0.071	0.068
ALV892-1 2µm_scan2	319	0.062	0.054
ALV892-1 2µm_scan6	986	0.048	0.042
ALV892-1 20µm_scan1	152	0.090	0.089
ALV892-1 20µm_scan2	319	0.088	0.088
ALV892-1 20µm_scan6	986	0.081	0.079
ALV892-1 50µm_scan1	304	0.097	0.097
ALV892-1 50µm_scan2	622	0.092	0.092

862
863 **Figure 10**. Normalized S-XANES spectra of MORB glasses JDF-46N and ALV892-1 with
864 repeat measurements in different locations using progressively greater photon flux densities.
865 Spectra have been vertically shifted for clarity. Spectra shown are examples from long sequences
866 of repeated analyses (20 repeated scans for JDF-46N; 2 – 6 repeated scans for ALV892-1).
867 Cumulative irradiation durations are listed on the right, and $S^{6+}/\Sigma S$ calculations using the peak
868 fitting approach with and without correcting for S^{4+} photo-reduction are compared. As in Figure

34

869   9, the ingrowth of S^{4+} (2476 – 2477.7 eV) and loss of S^{6+} (2480.5 – 2483.3 eV) is increasingly

870   apparent during longer analyses and those with more focused beams. Note that S^{4+} corrections do

871   not reproduce the $S^{6+}/\Sigma S$ observed with low photon density measurements, indicating that

872   challenge of applying beam damage corrections in reduced glasses with overlapping S^{2-} and S^{4+}

873   peak areas. Reference peak position lines may vary slightly between samples.

874

875   We also observe S^{6+} to S^{4+} photo-reduction during S-XANES analyses of low-H_2O

876   basaltic MI samples from the 2018 lower East Rift Zone (LERZ) fissure eruption of Kīlauea

877   Volcano, HI (≤0.3 wt% H_2O [Lerner et al., in revision]). Depending on the degree of

878   atmospheric interaction prior to quenching, the Kīlauea olivine-hosted MI range from reduced to

879   highly oxidized (FMQ -0.7 to +2.4; Lerner, 2020). S-XANES beam damage occurs in Kīlauea

880   MI throughout this wide range of oxidation states (Figure 11). The S^{6+} to S^{4+} photo-reduction

881   during X-ray irradiation in Kīlauea MI and in MORB glasses is particularly interesting because

882   these low-H_2O ocean island basalt (OIB) and MORB glasses are stable during Fe-XANES

883   measurements (Figure 11), having Φ values ≤0.1 (Table 1). These observations highlight that

884   major (e.g., iron) and minor (e.g., sulfur) elements may have different susceptibilities to X-ray

885   induced beam damage (Gonçalves Ferreira et al., 2013). Alternatively or additionally, the

886   different responses of iron and sulfur during irradiation may be related to their behavior as non-

887   volatile and volatile elements, or to the ratio of redox couples (e.g., S/Fe concentration ratios)

888   (Hughes et al., 2020).

889
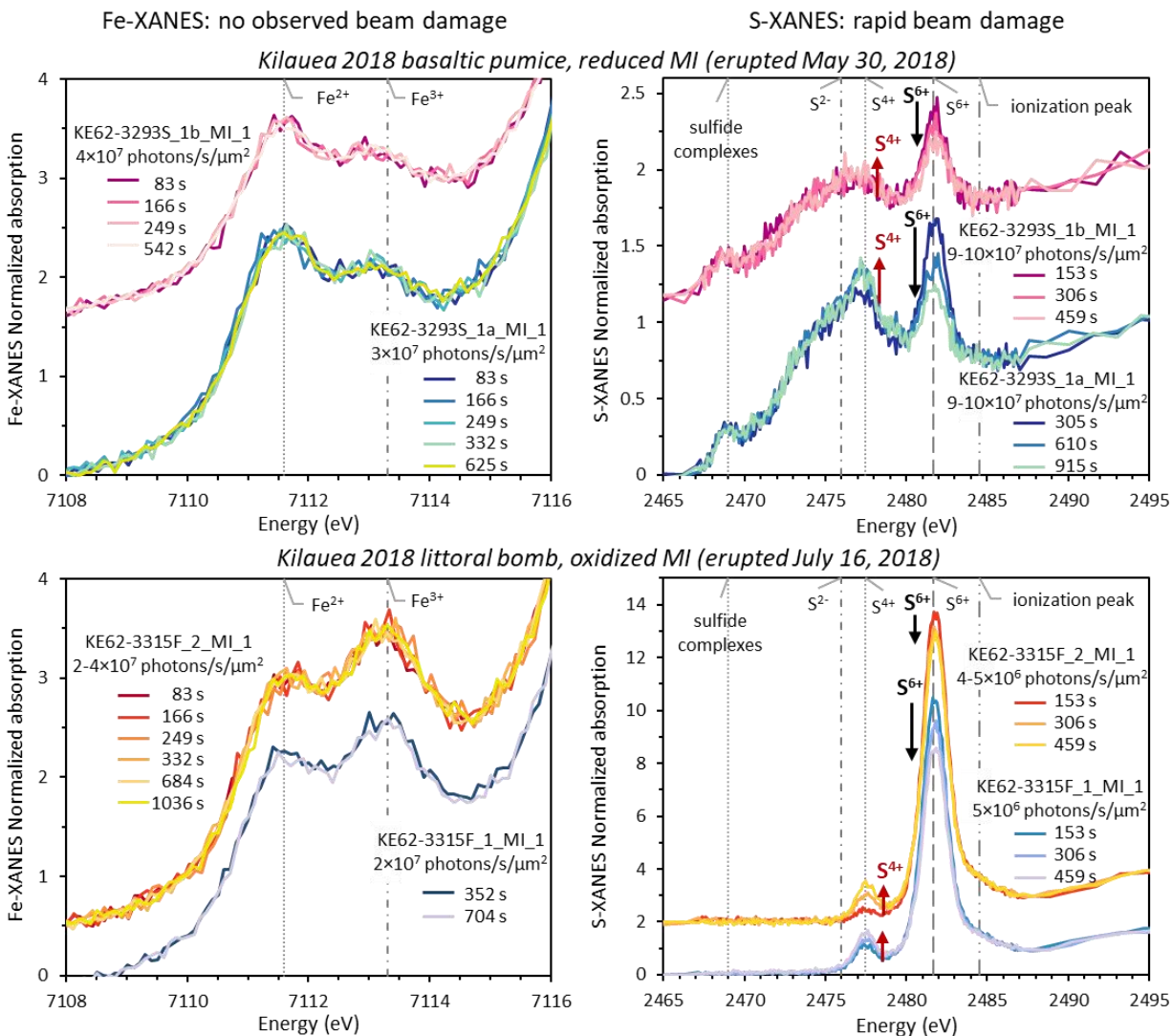
Figure 11. Four MI from the Kīlauea 2018 LERZ eruption were analyzed by both Fe- and S-XANES and exhibit differing susceptibilities to beam damage. Fe-XANES *(left)* and S-XANES *(right)* analyses were conducted in different locations within the same MI. Repeated rapid analyses were conducted for each technique, as described in the text, and the cumulative ending time in seconds (s) for successive scans are shown. Melt inclusions in both reduced, rapidly quenched basaltic pumice (KE62-3293S, *top*) and oxidized littoral bomb samples (KE62-3315F, *bottom*) exhibit no Fe^{2+} to Fe^{3+} photo-oxidation during repeat measurements, but the same MI undergo rapid S^{6+} to S^{4+} photo-reduction during S-XANES analyses. All MI contain ≤0.3 wt% H_2O and have Φ <0.1. Spot sizes were 10×10 um for Fe-XANES and 10×10 or 20×20 um for S-XANES resulting in photon flux densities of $2 - 4 \times 10^7$ and $4 - 10 \times 10^7$ photons/s/μm^2 for Fe- and S-XANES measurements, respectively. Vertical lines are approximate reference peak positions, which may vary slightly between samples.

904   **2.3.5 Discussion and summary**

905   The S-XANES peak fitting calibration and the determination of the S^{4+} to S^{6+} intensity

906   scaling factor could be improved with calibrations that include different compositions beyond the

907   basalts tested here (experimental glasses of Jugo et al. [2010] and Chowdhury and Dasgupta

908   [2019]). In particular, the concentration of Ca and Fe^{2+} may exert some control on sulfur

909   speciation at given fO_2 conditions and potentially on beam damage susceptibility in glasses (Graz

910   et al., 2007; Klimm et al., 2012a,b). H_2O-content may also play a role in S-XANES beam

911   damage susceptibility (Wilke et al., 2008) as it does in Fe-XANES photo-oxidation (Cottrell et

912   al., 2018). As an example, calculations of sulfur speciation in MORB glasses using the S^{4+} to S^{6+}

913   scaling factor of 1.2 to account for sulfur photo-reduction result in systematically lower $S^{6+}/\Sigma S$

914   for progressively more beam damaged analyses (from 0.09 to 0.03 $S^{6+}/\Sigma S$) (Figures 9, 10). This

915   indicates that the S^{4+} to S^{6+} scaling factor is likely larger for anhydrous, reduced basalt than what

916   we have determined for hydrous, oxidized basaltic glass. A S^{4+} to S^{6+} scaling factor of >3 is

917   required to equate the $S^{6+}/\Sigma S$ of highly beam damaged MORB analyses with the undamaged

918   measurements made using very low photon flux densities. However, we note that fitting the S^{4+}

919   peak is challenging in more reduced samples due to the overlap of the dominant S^{2-} peak with the

920   relatively minor S^{4+} peak, and we might be under-fitting the S^{4+} peak in the MORB spectra.

921   Additionally, in samples with mixed sulfur speciation, the slight beam damage-induced energy

922   increase in the 2470 – 2475 eV range (Figure 8 inset) would be completely masked by, and

923   included within, the broad S^{2-} peak area. Further characterizing the complete range of sulfur

924   complexing and valence changes during beam damage will be important for further improving S-

925   XANES correction methods. The uncertainties in the S^{4+} to S^{6+} intensity corrections underscore

926   that the foremost approach during S-XANES measurements should be to minimize beam damage

927   as much as possible, so that the overall uncertainties stemming from any S^{4+} corrections are

928   small.

929   In summary, S-XANES beam damage can occur in both hydrous and anhydrous silicate

930   glasses, but can be identified through repeat rapid scans by the presence and growth of a S^{4+}

931   peak. If beam damage is found to occur, we suggest focusing on the least damaged spectra for

932   each measurement, and then applying a S^{4+} to S^{6+} scaling factor to restore S^{4+} signal to the

933   original S^{6+} intensity. In high-sulfur samples, where signal intensity is sufficient even with rapid

934   scans, this is the ideal approach as beam damage is first limited and then restored to a good

935 approximation of original S^{6+} intensity. Low-sulfur samples may require merging multiple rapid

936 scans to obtain quantifiable spectra, despite the longer cumulative analysis time inducing more

937 photo-reduction. In long duration or merged scans, irradiation-induced S^{4+} signal can still be

938 restored to S^{6+} intensity, and although this introduces greater uncertainty (due to imprecisely

939 known S^{4+} to S^{6+} scaling factors), it is still a better approach than not applying any beam damage

940 correction. In highly oxidized samples lacking S^{2-}, accounting for S^{4+} is less important as it can

941 simply be assumed that all sulfur was originally present as S^{6+}. However, in samples with mixed

942 sulfur speciation, separating any S^{4+} photo-reduction signal from the overlapping S^{2-} peak, and

943 restoring the S^{4+} to original S^{6+} is important in accurately determining the initial sulfur speciation

944 of the glass.

945

946 **3.1 Identifying Fe-oxide nanolite crystals in Fe-XANES spectra**

947 In addition to beam damage concerns during XANES analyses of glasses, the possible

948 cryptic occurrence of nanolite crystals in glasses must also be considered to avoid spurious

949 interpretations of XANES spectra. Nanolites are minerals in the sub-micron range that are

950 typically undecipherable with optical microscopes or even with electron microscopes, but can

951 form in MI during quenching under certain conditions. In some settings, dispersed nanolite

952 crystals become large enough to appear as a fine "dust" within MI (Danyushevsky et al., 2002;

953 Wallace et al., 2003). It has been suggested that Fe-oxides and sulfides may form in MI during

954 cooling and/or diffusive H_2O-loss (Danyushevsky et al., 2002; Rowe et al., 2007; Di Genova et

955 al., 2017, 2018; Head et al., 2018). Di Genova et al. (2017, 2018) observe that Fe-oxide

956 (magnetite) nanolites preferentially occur in H_2O-rich glasses ($\geq$2.5 wt% H_2O) across a range of

957 compositions, suggesting that high H_2O promotes nanolite formation during quenching. This

958 might occur, for example, because increased H_2O lowers the glass transition temperature,

959 resulting in a larger cooling interval in the liquid state for H_2O-rich melts (Deubener et al.,

960 2003). The presence of nanolites complicates XANES, Raman, and EPMA redox measurements

961 in glasses because the bonding coordination in nanolite minerals may lead to different

962 relationships between ion abundances and signal intensities compared to calibrated relationships

963 in glasses.

964   Fortunately, the short-range ordering of iron and sulfur in mineral phases can be readily

965   detected via XANES and Raman spectral techniques (Wilke et al., 2006; Di Genova et al., 2017,

966   2018; Head et al., 2018). Magnetite nanolites have been spectrally identified by Raman

967   measurements in MI from basalts, dacites, and trachytes containing >4.5 wt% FeO^T and ≥2.5

968   wt% H_2O (Di Genova et al., 2017, 2018). Magnetite nanolite abundance correlates with more

969   oxidized (EPMA-calculated) redox states of MI (Hughes et al., 2018), although it is unclear if

970   nanolites actually form in more oxidized MI, or rather that the presence of nanolites affects the

971   redox quantification. Ni-, V-, and S-XANES have been used by Farges et al. (2001) to identify

972   Ni-bearing nanolites in hydrous albitic experimental glasses (≥ 4.5 wt% H_2O) and by Head et al.

973   (2018) to identify V- and S-bearing spinel and sulfide nanolites in natural basaltic MI from

974   Nyamuragira volcano (D.R. Congo). Finally, Fe-XANES has been used by Wilke et al. (2006) to

975   identify the formation of Fe-oxide nanolites during the slow quenching of hydrous haplogranitic

976   experimental glasses (where 0.06 – 1.5 μm diameter maghemite nanolites were confirmed by

977   TEM).

978   Here, we build on the observations of Wilke et al. (2006) and show that Fe-XANES

979   measurements can identify the cryptic occurrence of Fe-oxide nanolites in naturally quenched,

980   optically glassy MI. We conducted Fe-XANES measurements of doubly-intersected dacitic-

981   rhyolitic MI from the 2006 eruption of Augustine Volcano (AK, USA) (Lerner, 2020) and of

982   basaltic MI from Cerro Negro (Nicaragua) (Gaetani et al., 2012). A number of these MI contain

983   a sharp absorption peak at ~7129.5 eV that is similar to the absorption edge feature observed in

984   magnetite phenocrysts from both Augustine and oxidized Kīlauea 2018 LERZ samples (Figure

985   12). This magnetite-like peak indicates increased crystalline ordering of iron in the glasses due to

986   Fe-oxide nanolites (Wilke et al., 2006). A magnetite-like peak was also observed in Fe-XANES

987   measurements of optically glassy quartz-hosted MI from Central Andean volcanic centers by

988   Grocke et al. (2016), who similarly considered this feature to indicate Fe-oxide nanolite

989   interference.

990   Melt inclusions in Augustine feldspar and pyroxene grains that contain Fe-oxide

991   (presumably magnetite or maghemite) nanolites are consistently a brown color, although no

992   distinct fine-scale crystals are observable with either optical or electron microscopes (Figures 12,

993   13). Optically colorless MI are also present in the same samples from Augustine, and these

994   colorless MI have smooth Fe-XANES absorption edge spectra that are indicative of glass with no

995   magnetite-like structure (Figures 12, 13). The occurrence of colorless and brown MI, even within

996   the same sample, has been long recognized, and the cause and importance of MI glass color has

997   been much debated. Although some studies have found that colorless MI contain lower H_2O and

998   higher CO_2 than co-occurring brown MI, other studies find negligible differences in volatiles or

999   major element compositions between different colored MI (Wallace et al., 1999; Myers et al.,

1000 2016; Myers, 2017). However, Fe-XANES analyses show that the color of Augustine MI

1001 consistently reflects the presence or absence of magnetite nanolites. These findings are consistent

1002 with observations of Fe-oxide (and other crystalline phases) nanolites causing the dark color of

1003 natural obsidian and rhyolitic glass (e.g., Sharp et al., 1996; Castro et al., 2005; Ma et al., 2007;

1004 Tuffen et al., 2021; Galoisy and Calas, 2021). Iron nanolite-bearing Augustine MI have highly

1005 variable calculated $Fe^{3+}/\Sigma Fe$, but in general, these MI are more Fe^{3+}-rich compared to colorless,

1006 nanolite-free MI from the same tephra sample (Lerner, 2020). However, it is again unclear

1007 whether this observation reflects an increased oxidation state within the nanolite-bearing MI or if

1008 it is a consequence of greater Fe^{3+} signal from the crystalline nanolite phases. Importantly, the

1009 presence of Fe-oxide nanolites may invalidate the Fe-XANES centroid energy to $Fe^{3+}/\Sigma Fe$

1010 calibrations for glasses. Until further research is undertaken to investigate such effects on

1011 XANES calibrations, spectra containing nanolite signatures should be interpreted cautiously. To

1012 help focus sample selection and avoid nanolite-induced complications during synchrotron

1013 analyses, Raman spectra could be acquired prior to XANES analyses to identify whether

1014 nanolites are present in target glasses (Di Genova et al., 2017, 2018).

1015   We note that many brown-colored MI in more basaltic compositions have clean glassy

1016 XANES spectra with no evidence of nanolites (e.g., many Kīlauea LERZ and southern Cascades

1017 olivine-hosted MI studied here), so MI color alone does not always indicate the presence of Fe-

1018 oxide nanolites. Future efforts to characterize compositional, temperature, and H_2O variations

1019 between co-occurring brown and colorless MI in the same units will better clarify the processes

1020 that govern Fe-oxide nanolite formation and MI glass color.

1021
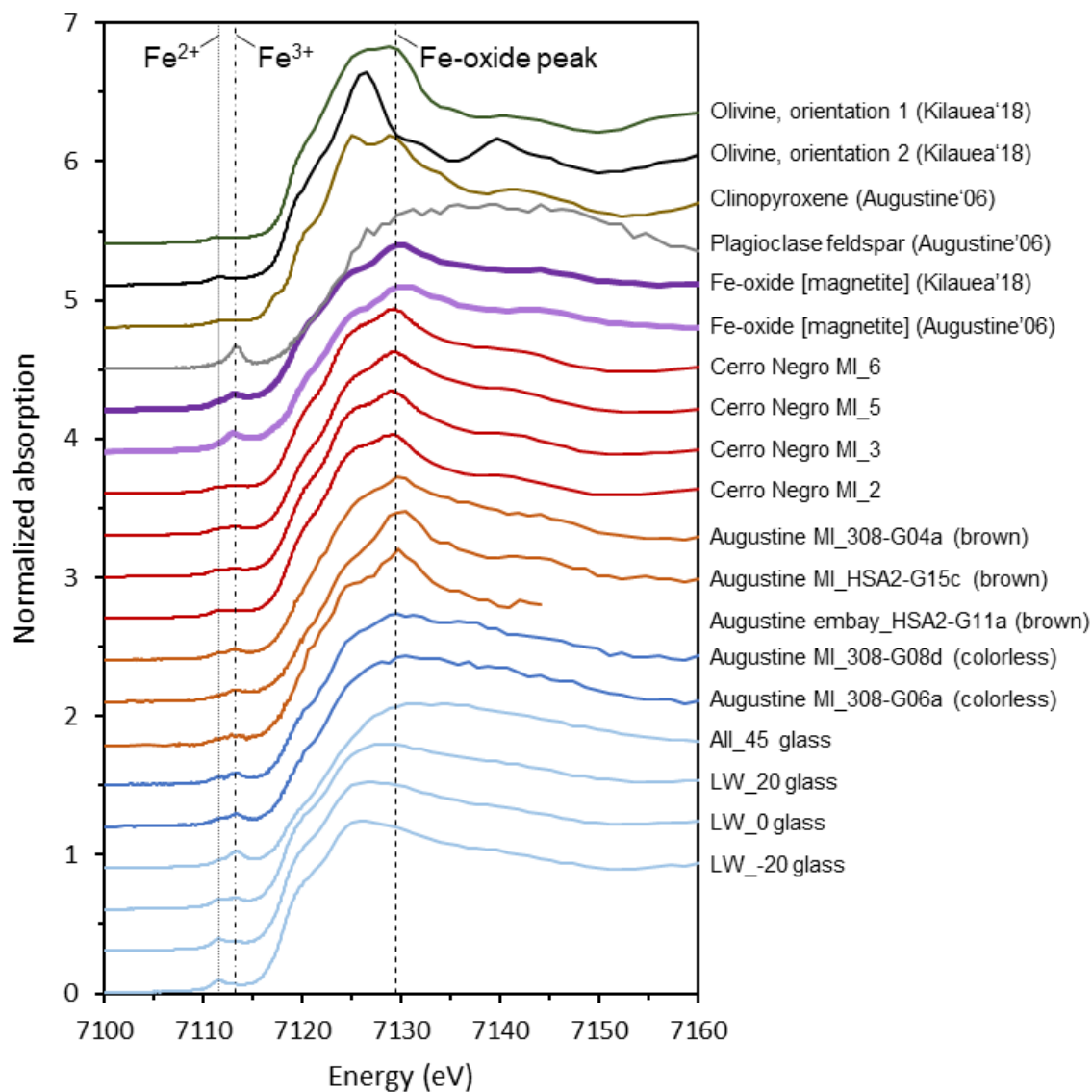
1022

Figure 12. Normalized Fe-XANES spectra of mineral spectra (olivine, clinopyroxene, feldspar, magnetite), reference glasses (LW series, AII_45; Cottrell et al., 2009), and doubly-intersected MI or melt embayment glasses from Augustine 2006 (samples shown in Figure 13) and Cerro Negro (see **Data supplement**). Brown-colored dacitic-rhyolitic glasses from Augustine (orange lines) have a prominent peak at ~7129.5 eV that closely resemble magnetite spectra (thick purple lines), indicating the presence of Fe-oxide nanolites. Cerro Negro olivine-hosted basaltic MI (red lines) also have a 7129.5 eV signature of magnetite nanolites. Colorless MI from Augustine (blue lines) have glassy spectra, similar to oxidized reference glasses LW_20 and AII_45 (FMQ +2 and +4.5, respectively). Spectra have been vertically shifted for clarity. The lines labeled Fe^{2+} and Fe^{3+} refer to the approximate peak positions of the first and second pre-edge doublet.

1033

1034

1035
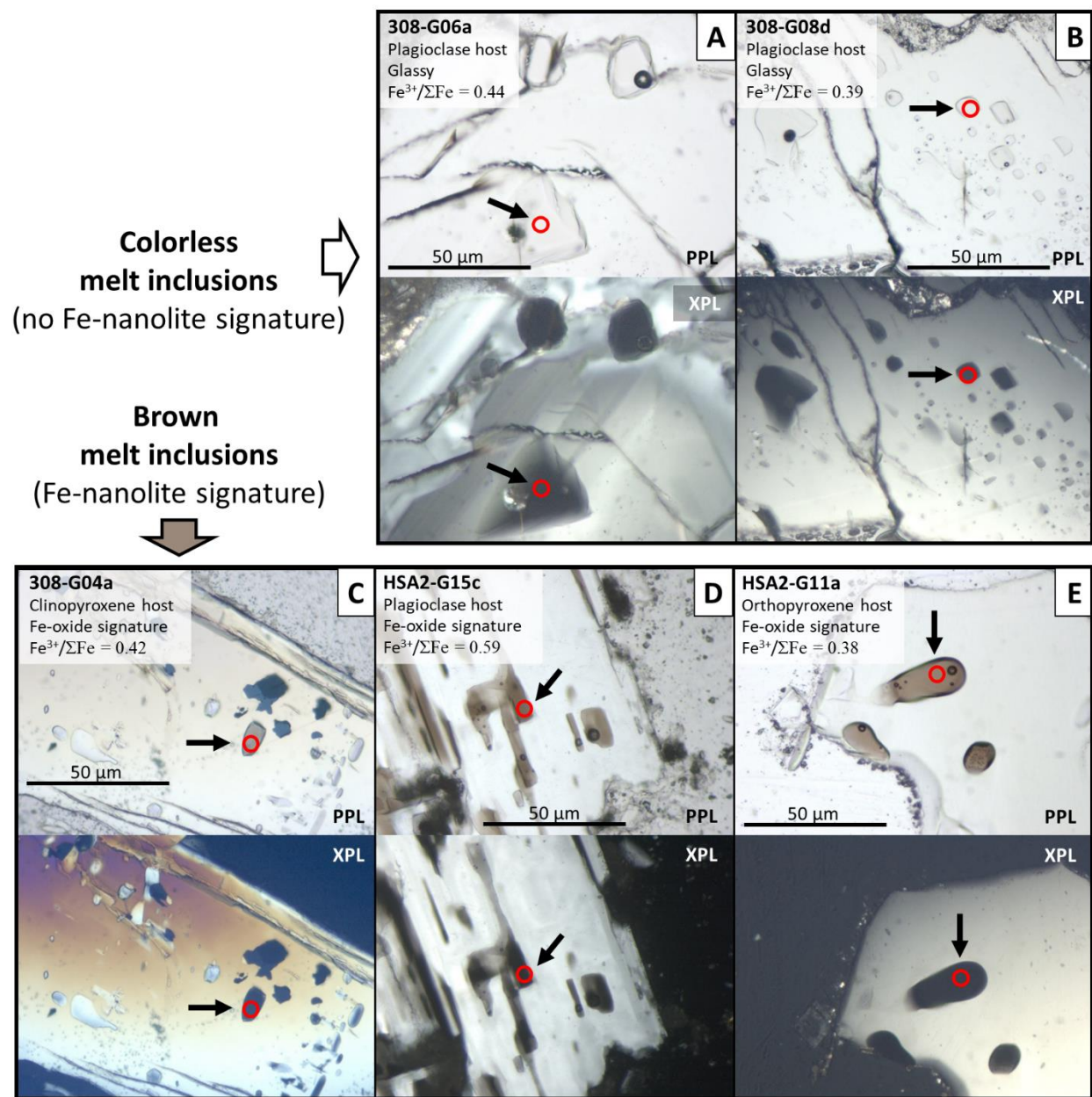
Figure 13. Doubly-intersected dacitic-rhyolitic MI (A, B, C, D) and melt embayments (E) erupted from Augustine in 2006. *(top)* Colorless glasses (A, B) and *(bottom)* brown glasses with Fe-oxide nanolite spectral signatures (C, D, E) are present in inclusions and embayments within plagioclase (A, B, D, E) and pyroxene (C). Each two-pane panel shows images with plane polarized light (PPL) and through crossed polarizers (XPL), with full glass extinction in XPL showing where MI are doubly-intersected for host-free Fe-XANES analysis. All Fe-XANES analyses were conducted with a 5×5 μm spot size (~1.4×10^8 photons/s/μm^2 flux densities), and spectra are shown in Figure 12. Photo-oxidation was not observed during repeated analyses in these glasses. Fe^{3+}/ΣFe was calculated from the felsic glass calibration of Fiege et al. (2017), although we note that the presence of Fe-oxide nanolites in the brown MI may invalidate such Fe^{3+}/ΣFe calculations.

1049

1050   **4.1 Conclusions and implications**

1051   Accurate XANES measurements are essential for inferring magma redox state from iron

1052   and sulfur valence states in quenched glasses. Using repeated, rapid Fe- and S-XANES

1053   measurements and implementing a new peak-fitting calibration for S-XANES, we have

1054   developed time-dependent corrections to identify and correct for beam damage during Fe- and S-

1055   XANES analyses of silicate glasses. Beam damage corrections for iron photo-oxidation and

1056   sulfur photo-reduction are determined for each individual analysis rather than applying

1057   generalized corrections. This allows versatility to account for composition differences and the

1058   effects of variable H_2O concentrations in MI that are commonly found in an individual tephra

1059   sample, which can influence beam damage susceptibility. Testing these beam damage correction

1060   methods on hydrous experimental basalts, we show that Fe- and S-XANES measurements can be

1061   reliably made even on beam-sensitive glasses. Additional studies of the mechanisms and

1062   compositional dependence of S-XANES beam damage could further improve the photo-

1063   reduction correction method that we have introduced here. Additionally, using Fe-XANES, we

1064   demonstrate the occurrence of cryptic Fe-oxide nanolites in naturally quenched MI. Melt

1065   inclusions containing nanolite phases may invalidate Fe- and S-XANES calibrations for

1066   elemental valence and speciation in glasses, and such spectra should be interpreted with caution.

1067   The analytical techniques presented here extend the ability to reliably measure iron

1068   valence and sulfur speciation in small and/or hydrous MI, which can undergo substantial beam

1069   damage during XANES analyses. These methods will allow further exploration of the redox

1070   behavior in hydrous systems, such as magmatic arcs and high-H_2O intraplate volcanic settings.

1071   Measurements of redox conditions in magmatic arc glasses are of particular interest to assess

1072   whether subduction inputs oxidize the sub-arc mantle and the relative importance of fO_2 in

1073   controlling volcanic degassing and the formation of porphyry copper ore deposits.

1074   We demonstrate that irradiation-induced changes in S-XANES spectra occur rapidly even

1075   in H_2O-poor MORB and OIB glasses that do not experience beam damage during Fe-XANES

1076   analysis. This raises the possibility that other multivalent trace element may similarly be subject

1077   to variation during X-ray analysis, even in relatively anhydrous glasses. The time-dependent

1078   analytical techniques presented here can be extended to XANES analyses of other multivalent

1079   trace elements, which are being increasingly applied to volcanic glasses (e.g., V-, Cr-, Cu-

1080   XANES; Sutton et al., 2020), to assess whether changes in valence or molecular complexing

1081   may be occurring during irradiation.

1082

Acknowledgements

1100

Author Contributions

1102   A.H.L. and M.J.M. conceived of the project and led sample preparation, analysis, data

1103   synthesis, and authoring. P.J.W., A.L., and M.N. aiding in project design, data interpretation, and

1104   manuscript editing. G.A.G., P.C., and R.D. aided in sample preparation and manuscript editing.

1105   **References**

1106   Anzures B. A., Parman S. W., Milliken R. E., Lanzirotti A. and Newville M. (2020) XANES
1107   spectroscopy of sulfides stable under reducing conditions. *American Mineralogist* **105**,
1108   375–381.

1109   Backnaes L., Stelling J., Behrens H., Goettlicher J., Mangold S., Verheijen O., Beerkens R. G. C.
1110   and Deubener J. (2008) Dissolution Mechanisms of Tetravalent Sulphur in Silicate Melts:
1111   Evidences from Sulphur K Edge XANES Studies on Glasses. *Journal of the American
1112   Ceramic Society* **91**, 721–727.

1113   Bajt S., Sutton S. R. and Delaney J. S. (1994) X-ray microprobe analysis of iron oxidation states
1114   in silicates and oxides using X-ray absorption near edge structure (XANES). *Geochimica
1115   et Cosmochimica Acta* **58**, 5209–5214.

1116   Baker D. R. and Moretti R. (2011) Modeling the solubility of sulfur in magmas: a 50-year old
1117   geochemical challenge. *Reviews in Mineralogy and Geochemistry* **73**, 167–213.

1118   Barnes J. D., Prather T. J., Cisneros M., Befus K., Gardner J. E. and Larson T. E. (2014) Stable
1119   chlorine isotope behavior during volcanic degassing of H_2O and CO_2 at Mono Craters,
1120   CA. *Bulletin of Volcanology* **76**, 805.

1121   Berry A. J., Danyushevsky L. V., O'Neill H. S. C., Newville M. and Sutton S. R. (2008)
1122   Oxidation state of iron in komatiitic melt inclusions indicates hot Archaean mantle.
1123   *Nature* **455**, 960.

1124   Berry A. J., O'Neill H. St. C., Jayasuriya K. D., Campbell S. J. and Foran G. J. (2003) XANES
1125   calibrations for the oxidation state of iron in a silicate glass. *American Mineralogist* **88**,
1126   967–977.

1127   Berry A. J., Stewart G. A., O'Neill H. S. C., Mallmann G. and Mosselmans J. F. W. (2018) A re-
1128   assessment of the oxidation state of iron in MORB glasses. *Earth and Planetary Science
1129   Letters* **483**, 114–123.

1130   Bonnin-Mosbah M., Métrich N., Susini J., Salomé M., Massare D. and Menez B. (2002) Micro
1131   X-ray absorption near edge structure at the sulfur and iron K-edges in natural silicate
1132   glasses. *Spectrochimica Acta Part B: Atomic Spectroscopy* **57**, 711–725.

1133   Bonnin-Mosbah M., Simionovici A. S., Métrich N., Duraud J.-P., Massare D. and Dillmann P.
1134   (2001) Iron oxidation states in silicate glass fragments and glass inclusions with a
1135   XANES micro-probe. *Journal of Non-Crystalline Solids* **288**, 103–113.

1136   Borisov A., Behrens H. and Holtz F. (2018) Ferric/ferrous ratio in silicate melts: A new model
1137   for 1 atm data with special emphasis on the effects of melt composition. *Contributions to
1138   Mineralogy and Petrology* **173**, 98.

Botcharnikov R. E., Linnen R. L., Wilke M., Holtz F., Jugo P. J. and Berndt J. (2011) High gold concentrations in sulphide-bearing magma under oxidizing conditions. *Nature Geosci* **4**, 112–115.

Brounce M. N., Boyce J., McCubbin F. M., Humphreys J., Reppart J., Stolper E. and Eiler J. (2019) The oxidation state of sulfur in lunar apatite. *American Mineralogist* **104**, 307–312.

Brounce M. N., Kelley K. A. and Cottrell E. (2014) Variations in $Fe^{3+}/\Sigma Fe$ of Mariana Arc basalts and mantle wedge fO_2. *Journal of Petrology* **55**, 2513–2536.

Brounce M. N., Stolper E. and Eiler J. (2017) Redox variations in Mauna Kea lavas, the oxygen fugacity of the Hawaiian plume, and the role of volcanic gases in Earth's oxygenation. *Proceedings of the National Academy of Sciences* **114**, 8997–9002.

Browaeys J. (2021) *Linear fit with both uncertainties in x and in y.*, MATLAB Central File Exchange.

Callegaro S., Geraki K., Marzoli A., Min A. D., Maneta V. and Baker D. R. (2020) The quintet completed: The partitioning of sulfur between nominally volatile-free minerals and silicate melts. *American Mineralogist* **105**, 697–707.

Carroll M. and Rutherford M. J. (1988) Sulfur speciation in hydrous experimental glasses of varying oxidation state–results from measured wavelength shifts of sulfur X-rays. *American Mineralogist* **73**, 845–9.

Castro J. M., Dingwell D. B., Nichols A. R. and Gardner J. E. (2005) New insights on the origin of flow bands in obsidian. In *Kinematics and dynamics of lava flows* (eds. M. Manga and G. Ventura). Special Papers-Geological Society of America. Boulder, Colo.; Geological Society of America; 1999. pp. 55–65.

Chowdhury P. and Dasgupta R. (2019) Effect of sulfate on the basaltic liquidus and Sulfur Concentration at Anhydrite Saturation (SCAS) of hydrous basalts–Implications for sulfur cycle in subduction zones. *Chemical Geology* **522**, 162–174.

Cottrell E., Birner S., Brounce M. N., Davis F. A., Waters L. E. and Kelley K. A. (2020) Oxygen Fugacity Across Tectonic Settings. In *Redox variables and mechanisms in magmatism and volcanism* (eds. D. R. Neuville and R. Moretti). AGU Geophysical Monograph. Wiley.

Cottrell E. and Kelley K. A. (2011) The oxidation state of Fe in MORB glasses and the oxygen fugacity of the upper mantle. *Earth and Planetary Science Letters* **305**, 270–282.

Cottrell E., Kelley K. A., Lanzirotti A. and Fischer R. A. (2009) High-precision determination of iron oxidation state in silicate glasses using XANES. *Chemical Geology* **268**, 167–179.

1173 Cottrell E., Lanzirotti A., Mysen B., Birner S., Kelley K. A., Botcharnikov R., Davis F. A. and
1174   Newville M. (2018) A Mössbauer-based XANES calibration for hydrous basalt glasses
1175   reveals radiation-induced oxidation of Fe. *American Mineralogist* **103**, 489–501.

1176 Danyushevsky L. V., McNeill A. W. and Sobolev A. V. (2002) Experimental and petrological
1177   studies of melt inclusions in phenocrysts from mantle-derived magmas: An overview of
1178   techniques, advantages and complications. *Chemical Geology* **183**, 5–24.

1179 Dauphas N., Roskosz M., Alp E. E., Neuville D. R., Hu M. Y., Sio C. K., Tissot F. L. H., Zhao
1180   J., Tissandier L. and Médard E. (2014) Magma redox and structural controls on iron
1181   isotope variations in Earth's mantle and crust. *Earth and Planetary Science Letters* **398**,
1182   127–140.

1183 Deubener J., Müller R., Behrens H. and Heide G. (2003) Water and the glass transition
1184   temperature of silicate melts. *Journal of Non-Crystalline Solids* **330**, 268–273.

1185 Di Genova D., Caracciolo A. and Kolzenburg S. (2018) Measuring the degree of "nanotilization"
1186   of volcanic glasses: Understanding syn-eruptive processes recorded in melt inclusions.
1187   *Lithos* **318**, 209–218.

1188 Di Genova D., Sicola S., Romano C., Vona A., Fanara S. and Spina L. (2017) Effect of iron and
1189   nanolites on Raman spectra of volcanic glasses: A reassessment of existing strategies to
1190   estimate the water content. *Chemical Geology* **475**, 76–86.

1191 Dyar M. D., McCanta M., Breves E., Carey C. J. and Lanzirotti A. (2016) Accurate predictions
1192   of iron redox state in silicate glasses: A multivariate approach using X-ray absorption
1193   spectroscopy. *American Mineralogist* **101**, 744–747.

1194 Elam W. T., Ravel B. D. and Sieber J. R. (2002) A new atomic database for X-ray spectroscopic
1195   calculations. *Radiation Physics and Chemistry* **63**, 121–128.

1196 Farges F., Lefrère Y., Rossano S., Berthereau A., Calas G. and Brown G. E. (2004) The effect of
1197   redox state on the local structural environment of iron in silicate glasses: a combined
1198   XAFS spectroscopy, molecular dynamics, and bond valence study. *Journal of Non-*
1199   *Crystalline Solids* **344**, 176–188.

1200 Farges F., Munoz M., Siewert R., Malavergne V., Brown G. E., Behrens H., Nowak M. and Petit
1201   P.-E. (2001) Transition elements in water-bearing silicate glasses/melts. part II. Ni in
1202   water-bearing glasses. *Geochimica et Cosmochimica Acta* **65**, 1679–1693.

1203 Fiege A., Holtz F., Shimizu N., Mandeville C. W., Behrens H. and Knipping J. L. (2014) Sulfur
1204   isotope fractionation between fluid and andesitic melt: An experimental study.
1205   *Geochimica et Cosmochimica Acta* **142**, 501–521.

1206 Fiege A., Ruprecht P., Simon A. C., Bell A. S., Göttlicher J., Newville M., Lanzirotti T. and
1207   Moore G. (2017) Calibration of Fe XANES for high-precision determination of Fe
1208   oxidation state in glasses: Comparison of new and existing results obtained at different
1209   synchrotron radiation sources. *American Mineralogist* **102**, 369–380.

1210 Fleet M. E., Liu X., Harmer S. L. and King P. L. (2005) Sulfur K-edge XANES spectroscopy:
1211   Chemical state and content of sulfur in silicate glasses. *The Canadian Mineralogist* **43**,
1212   1605–1618.

1213 Gaborieau M., Laubier M., Bolfan-Casanova N., McCammon C. A., Vantelon D., Chumakov A.
1214   I., Schiavi F., Neuville D. R. and Venugopal S. (2020) Determination of $Fe^{3+}/\Sigma Fe$ of
1215   olivine-hosted melt inclusions using Mössbauer and XANES spectroscopy. *Chemical*
1216   *Geology* **547**, 119646.

1217 Gaetani G. A., O'Leary J. A., Shimizu N., Bucholz C. E. and Newville M. (2012) Rapid
1218   reequilibration of H_2O and oxygen fugacity in olivine-hosted melt inclusions. *Geology*
1219   **40**, 915–918.

1220 Galoisy L. and Calas G. (2021) The unique speciation of iron in calc-alkaline obsidians.
1221   *Chemical Geology* **559**, 119925.

1222 Galoisy L., Calas G. and Arrio M. A. (2001) High-resolution XANES spectra of iron in minerals
1223   and glasses: structural information from the pre-edge region. *Chemical geology* **174**,
1224   307–319.

1225 Gonçalves Ferreira P., de Ligny D., Lazzari O., Jean A., Gonzalez O. C. and Neuville D. R.
1226   (2013) Photoreduction of iron by a synchrotron X-ray beam in low iron content soda-lime
1227   silicate glasses. *Chemical Geology* **346**, 106–112.

1228 Graz Y., Scaillet B., Pichavant M. and Gaillard F. (2007) The effect of sulfur on the Fe^{2+}/Fe^{3+}
1229   ratio of MORB and its implications for the redox state of the mantle.

1230 Grocke S. B., Cottrell E., de Silva S. and Kelley K. A. (2016) The role of crustal and eruptive
1231   processes versus source variations in controlling the oxidation state of iron in Central
1232   Andean magmas. *Earth and Planetary Science Letters* **440**, 92–104.

1233 Head E., Lanzirotti A., Newville M. and Sutton S. (2018) Vanadium, sulfur, and iron valences in
1234   melt inclusions as a window into magmatic processes: A case study at Nyamuragira
1235   volcano, Africa. *Geochimica et Cosmochimica Acta* **226**, 149–173.

1236 Helz R. T., Cottrell E., Brounce M. N. and Kelley K. A. (2017) Olivine-melt relationships and
1237   syneruptive redox variations in the 1959 eruption of Kīlauea Volcano as revealed by
1238   XANES. *Journal of Volcanology and Geothermal Research* **333**, 1–14.

1239 Hughes E. C., Buse B., Kearns S. L., Blundy J. D., Kilgour G., Mader H. M., Brooker R. A.,
1240   Balzer R., Botcharnikov R. E. and Di Genova D. (2018) High spatial resolution analysis
1241   of the iron oxidation state in silicate glasses using the electron probe. *American*
1242   *Mineralogist: Journal of Earth and Planetary Materials* **103**, 1473–1486.

1243 Hughes E. C., Buse B., Kearns S. L., Brooker R. A., Di Genova D., Kilgour G., Mader H. M. and
1244   Blundy J. D. (2020) The microanalysis of iron and sulphur oxidation states in silicate
1245   glass-Understanding the effects of beam damage. In *IOP Conference Series: Materials*
1246   *Science and Engineering* IOP Publishing. p. 012014.

1247 Jarosewich E., Nelen J. A. and Norberg J. A. (1980) Reference samples for electron microprobe
1248   analysis. *Geostandards Newsletter* **4**, 43–47.

1249 Jégo S. and Dasgupta R. (2014) The fate of sulfur during fluid-present melting of subducting
1250   basaltic crust at variable oxygen fugacity. *Journal of Petrology* **55**, 1019–1050.

1251 Jugo P. J. (2009) Sulfur content at sulfide saturation in oxidized magmas. *Geology* **37**, 415–418.

1252 Jugo P. J., Wilke M. and Botcharnikov R. E. (2010) Sulfur K-edge XANES analysis of natural
1253   and synthetic basaltic glasses: Implications for S speciation and S content as function of
1254   oxygen fugacity. *Geochimica et Cosmochimica Acta* **74**, 5926–5938.

1255 Kelley K. A. and Cottrell E. (2012) The influence of magmatic differentiation on the oxidation
1256   state of Fe in a basaltic arc magma. *Earth and Planetary Science Letters* **329–330**, 109–
1257   121.

1258 Kelley K. A. and Cottrell E. (2009) Water and the oxidation state of subduction zone magmas.
1259   *Science* **325**, 605–607.

1260 Kent A. J. (2008) Melt inclusions in basaltic and related volcanic rocks. *Reviews in Mineralogy
1261   and Geochemistry* **69**, 273–331.

1262 Klimm K., Kohn S. C. and Botcharnikov R. E. (2012a) The dissolution mechanism of sulphur in
1263   hydrous silicate melts. II: Solubility and speciation of sulphur in hydrous silicate melts as
1264   a function of fO$_2$. *Chemical Geology* **322**, 250–267.

1265 Klimm K., Kohn S. C., O'Dell L. A., Botcharnikov R. E. and Smith M. E. (2012b) The
1266   dissolution mechanism of sulphur in hydrous silicate melts. I: Assessment of analytical
1267   techniques in determining the sulphur speciation in iron-free to iron-poor glasses.
1268   *Chemical Geology* **322**, 237–249.

1269 Konecke B. A., Fiege A., Simon A. C., Parat F. and Stechern A. (2017) Co-variability of S^{6+},
1270   S^{4+}, and S^{2-} in apatite as a function of oxidation state: Implications for a new
1271   oxybarometer. *American Mineralogist* **102**, 548–557.

1272 Kraft S., Stümpel J., Becker P. and Kuetgens U. (1996) High resolution x-ray absorption
1273   spectroscopy with absolute energy calibration for the determination of absorption edge
1274   energies. *Review of Scientific Instruments* **67**, 681–687.

1275 Kress V. C. and Carmichael I. S. (1991) The compressibility of silicate liquids containing Fe$_2$O$_3$
1276   and the effect of composition, temperature, oxygen fugacity and pressure on their redox
1277   states. *Contributions to Mineralogy and Petrology* **108**, 82–92.

1278 Kuehn S. C., Froese D. G., Shane P. A. R. and INTAV Intercomparison Participants (2011) The
1279   INTAV intercomparison of electron-beam microanalysis of glass by tephrochronology
1280   laboratories: results and recommendations. *Quaternary International* **246**, 19–47.

1281 Lanzirotti A., Lee L., Head E., Sutton S. R., Newville M., McCanta M., Lerner A. H. and
1282   Wallace P. J. (2019) Direct measurements of copper speciation in basaltic glasses:
1283   understanding the relative roles of sulfur and oxygen in copper complexation in melts.
1284   *Geochimica et Cosmochimica Acta* **267**, 164–178.

1285 Lerner A. H. (2020) The depths and locations of magma reservoirs and their consequences for
1286   the behavior of sulfur and volcanic degassing. Ph.D. Thesis, University of Oregon.

1287 Lerner A. H., Wallace P. J., Shea T., Mourey A. J., Kelly P. J., Nadeau P. A., Elias T., Kern C.,
1288   Clor L. E., Gansecki C., Lee R. L., Moore L. R. and Werner C. A. (2021) The petrologic
1289   and degassing behavior of sulfur and other magmatic volatiles from the 2018 eruption of
1290   Kīlauea, Hawaiʻi: melt concentrations, magma storage depths, and magma recycling. *Bull*
1291   *Volcanol* **83**, 43.

1292 Li D., Bancroft G. M., Kasrai M., Fleet M. E., Feng X. and Tan K. (1995) S K- and L-edge X-
1293   ray absorption spectroscopy of metal sulfides and sulfates; applications in mineralogy
1294   and geochemistry. *The Canadian Mineralogist* **33**, 949–960.

1295 Ma C., Rossman G. R. and Miller J. A. (2007) The Origin of Color in "Fire" Obsidian. *The*
1296   *Canadian Mineralogist* **45**, 551–557.

1297 Manceau A. and Nagy K. L. (2012) Quantitative analysis of sulfur functional groups in natural
1298   organic matter by XANES spectroscopy. *Geochimica et Cosmochimica Acta* **99**, 206–
1299   223.

1300 Masotta M. and Keppler H. (2015) Anhydrite solubility in differentiated arc magmas.
1301   *Geochimica et Cosmochimica Acta* **158**, 79–102.

1302 Matjuschkin V., Blundy J. D. and Brooker R. A. (2016) The effect of pressure on sulphur
1303   speciation in mid-to deep-crustal arc magmas and implications for the formation of
1304   porphyry copper deposits. *Contributions to Mineralogy and Petrology* **171**, 66.

1305 McCanta M. C., Dyar M. D., Lanzirotti A., Newville M. and Breitenfeld L. B. (2019) In-situ
1306   mapping of ferric iron variations in lunar glasses using X-ray absorption spectroscopy.
1307   *American Mineralogist* **104**, 453–458.

1308 McCanta M. C., Dyar M. D., Rutherford M. J., Lanzirotti A., Sutton S. R. and Thomson B. J.
1309   (2017) In situ measurement of ferric iron in lunar glass beads using Fe-XAS. *Icarus* **285**,
1310   95–102.

1311 Métrich N., Berry A. J., O'Neill H. S. C. and Susini J. (2009) The oxidation state of sulfur in
1312   synthetic and natural glasses determined by X-ray absorption spectroscopy. *Geochimica*
1313   *et Cosmochimica Acta* **73**, 2382–2399.

1314 Métrich N., Bonnin-Mosbah M., Susini J., Menez B. and Galoisy L. (2002) Presence of sulfite
1315   (SIV) in arc magmas: Implications for volcanic sulfur emissions. *Geophysical Research*
1316   *Letters* **29**, 33-1-33–4.

1317 Métrich N. and Wallace P. J. (2008) Volatile abundances in basaltic magmas and their degassing
1318   paths tracked by melt inclusions. *Reviews in Mineralogy and Geochemistry* **69**, 363–402.

1319 de Moor J. M., Fischer T. P., Sharp Z. D., King P. L., Wilke M., Botcharnikov R. E., Cottrell E.,
1320   Zelenski M., Marty B., Klimm K., Rivard C. and Ayalew D. (2013) Sulfur degassing at
1321   Erta Ale (Ethiopia) and Masaya (Nicaragua) volcanoes: Implications for degassing
1322   processes and oxygen fugacities of basaltic systems. *Geochemistry, Geophysics,*
1323   *Geosystems* **14**, 4076–4108.

1324 Moussallam Y., Edmonds M., Scaillet B., Peters N., Gennaro E., Sides I. and Oppenheimer C.
1325   (2016) The impact of degassing on the oxidation state of basaltic magmas: A case study
1326   of Kīlauea volcano. *Earth and Planetary Science Letters* **450**, 317–325.

1327 Moussallam Y., Longpré M.-A., McCammon C., Gomez-Ulla A., Rose-Koga E. F., Scaillet B.,
1328   Peters N., Gennaro E., Paris R. and Oppenheimer C. (2019) Mantle plumes are oxidised.
1329   *Earth and Planetary Science Letters* **527**, 115798.

1330 Moussallam Y., Oppenheimer C., Scaillet B., Gaillard F., Kyle P., Peters N., Hartley M., Berlo
1331   K. and Donovan A. (2014) Tracking the changing oxidation state of Erebus magmas,
1332   from mantle to surface, driven by magma ascent and degassing. *Earth and Planetary*
1333   *Science Letters* **393**, 200–209.

1334 Muth M. J. and Wallace P. J. (2021) Slab-derived sulfate generates oxidized basaltic magmas in
1335   the southern Cascade arc (California, USA). *Geology*.

1336 Myers M. L. (2017) Storage, ascent, and release of silicic magma in caldera-forming eruptions.
1337   PhD Thesis, University of Oregon.

1338 Myers M. L., Wallace P. J., Wilson C. J., Morter B. K. and Swallow E. J. (2016) Prolonged
1339   ascent and episodic venting of discrete magma batches at the onset of the Huckleberry
1340   Ridge supereruption, Yellowstone. *Earth and Planetary Science Letters* **451**, 285–297.

1341 Nash W. M., Smythe D. J. and Wood B. J. (2019) Compositional and temperature effects on
1342   sulfur speciation and solubility in silicate melts. *Earth and Planetary Science Letters* **507**,
1343   187–198.

1344 Newville M. (2013) Larch: An analysis package for XAFS and related spectroscopies. In *Journal*
1345   *of Physics: Conference Series* IOP Publishing. p. 012007.

1346 O'Neill H. S. C., Berry A. J. and Mallmann G. (2018) The oxidation state of iron in Mid-Ocean
1347   Ridge Basaltic (MORB) glasses: Implications for their petrogenesis and oxygen
1348   fugacities. *Earth and Planetary Science Letters* **504**, 152–162.

1349 Osborn E. F. (1959) Role of oxygen pressure in the crystallization and differentiation of basaltic
1350   magma. *Am J Sci* **257**, 609–647.

1351 Papike J. J., Simon S. B., Burger P. V., Bell A. S., Shearer C. K. and Karner J. M. (2016)
1352   Chromium, vanadium, and titanium valence systematics in Solar System pyroxene as a

1353   recorder of oxygen fugacity, planetary provenance, and processes. *American*
1354   *Mineralogist* **101**, 907–918.

1355 Paris E., Giuli G., Carroll M. R. and Davoli I. (2001) The valence and speciation of sulfur in
1356   glasses by X-ray absorption spectroscopy. *The Canadian Mineralogist* **39**, 331–339.

1357 Ravel B. and Newville M. (2005) ATHENA, ARTEMIS, HEPHAESTUS: data analysis for X-
1358   ray absorption spectroscopy using IFEFFIT. *Journal of synchrotron radiation* **12**, 537–
1359   541.

1360 Righter K., Danielson L. R., Pando K., Morris R. V., Graff T. G., Agresti D. G., Martin A. M.,
1361   Sutton S. R., Newville M. and Lanzirotti A. (2013) Redox systematics of martian
1362   magmas with implications for magnetite stability. *American Mineralogist* **98**, 616–628.

1363 Rose T. and Brown C. (2017) Status of the Smithsonian Microbeam Standards 2017 With a
1364   Discussion of the Venerable VG-2 Basalt Glass. *Microscopy and Microanalysis* **23**, 498–
1365   499.

1366 Rose-Koga E. F., Bouvier A.-S., Gaetani G. A., Wallace P. J., Allison C. M., Andrys J. A., de la
1367   Torre CA A., Barth A., Bodnar R. J., Ajj B. G., Butters, Castillejo A., Chilson-Parks B.,
1368   Choudhary B. R., Cluzel N., Cole M., Cottrell E., Daly A., Danyushevsky L. V., Cl D.,
1369   Drignon M. J., France L., Gaborieau M., Garcia M. O., Gatti E., Genske F. S., Hartley,
1370   Hughes E. C., Iveson A. A., Johnson E. R., Jones M., Kagoshima T., Katzir Y.,
1371   Kawaguchi M., Kawamoto T., Kelley K. A., Koornneef J. M., Kurz, Laubier M., Layne
1372   G. D., Lerner A., Lin K.-Y., Liu P.-P., Lorenzo-Merino A., Luciani N., Magalhães N.,
1373   Marschall H. R., Michael P. J., Monteleone B. D., Moore L. R., Moussallam Y., Muth
1374   M., Myers M. L., Narváez D. F., Navon O., Newcombe, Arl N., Nielsen R. L., Pamukcu
1375   A., Plank T., Rasmussen D. J., Roberge J., Schiavi F., Schwartz, Kei S., Shimizu K.,
1376   Shimizu N., Thomas J. B., Thompson G. T., Tucker J. M., Ustunisik G., Waelkens C.,
1377   Zhang Y. and Zhou T. (2021) Silicate melt inclusions in the new millennium: A review
1378   of recommended practices for preparation, analysis, and data presentation. *Chemical*
1379   *Geology*, 120145.

1380 Rowe M. C., Kent A. J. and Nielsen R. L. (2007) Determination of sulfur speciation and
1381   oxidation state of olivine hosted melt inclusions. *Chemical Geology* **236**, 303–322.

1382 Schreiber H. D., Merkel Jr R. C., Schreiber V. L. and Balazs G. B. (1987) Mutual interactions of
1383   redox couples via electron exchange in silicate melts: models for geochemical melt
1384   systems. *Journal of Geophysical Research: Solid Earth* **92**, 9233–9245.

1385 Sharp T. G., Stevenson R. J. and Dingwell D. B. (1996) Microlites and "nanolites" in rhyolitic
1386   glass: microstructural and chemical characterization. *Bull Volcanol* **57**, 631–640.

1387 Shorttle O., Moussallam Y., Hartley M. E., Maclennan J., Edmonds M. and Murton B. J. (2015)
1388   Fe-XANES analyses of Reykjanes Ridge basalts: Implications for oceanic crust's role in
1389   the solid Earth oxygen cycle. *Earth and Planetary Science Letters* **427**, 272–285.

Sutton S. R., Lanzirotti A., Newville M., Dyar M. D. and Delaney J. (2020) Oxybarometry and valence quantification based on microscale X-ray absorption fine structure (XAFS) spectroscopy of multivalent elements. *Chemical Geology* **531**, 119305.

Sutton S. R., Lanzirotti A., Newville M., Rivers M. L., Eng P. and Lefticariu L. (2017) Spatially resolved elemental analysis, spectroscopy and diffraction at the GSECARS Sector at the Advanced Photon Source. *Journal of environmental quality* **46**, 1158–1165.

Tassara S., Reich M., Cannatelli C., Konecke B. A., Kausel D., Morata D., Barra F., Simon A. C., Fiege A. and Morgado E. (2020) Post-melting oxidation of highly primitive basalts from the southern Andes. *Geochimica et Cosmochimica Acta* **273**, 291–312.

Tuffen H., Flude S., Berlo K., Wadsworth F. and Castro J. (2021) Obsidian. In *Encyclopedia of Geology (Second Edition)* (eds. D. Alderton and S. A. Elias). Academic Press, Oxford. pp. 196–208.

Wallace P. J., Anderson Jr A. T. and Davis A. M. (1999) Gradients in H_2O, CO_2, and exsolved gas in a large-volume silicic magma system: Interpreting the record preserved in melt inclusions from the Bishop Tuff. *Journal of Geophysical Research: Solid Earth* **104**, 20097–20122.

Wallace P. J. and Carmichael I. S. E. (1994) S speciation in submarine basaltic glasses as determined by measurements of $SK\alpha$ X-ray wavelength shifts. *American Mineralogist* **79**, 161–167.

Wallace P. J., Dufek J., Anderson A. T. and Zhang Y. (2003) Cooling rates of Plinian-fall and pyroclastic-flow deposits in the Bishop Tuff: inferences from water speciation in quartz-hosted glass inclusions. *Bulletin of Volcanology* **65**, 105–123.

Wallace P. J., Plank T., Bodnar R. J., Gaetani G. A. and Shea T. (2021) Olivine-Hosted Melt Inclusions: A Microscopic Perspective on a Complex Magmatic World. *Annual Review of Earth and Planetary Sciences* **49**.

Watkins J. M., Gardner J. E. and Befus K. S. (2017) Nonequilibrium degassing, regassing, and vapor fluxing in magmatic feeder systems. *Geology* **45**, 183–186.

Waychunas G. A., Apted M. J. and Brown G. E. (1983) X-ray K-edge absorption spectra of Fe minerals and model compounds: Near-edge structure. *Phys Chem Minerals* **10**, 1–9.

Weaver S. L., Wallace P. J. and Johnston A. D. (2011) A comparative study of continental vs. intraoceanic arc mantle melting: Experimentally determined phase relations of hydrous primitive melts. *Earth and Planetary Science Letters* **308**, 97–106.

Wilke M., Farges F., Partzsch G. M., Schmidt C. and Behrens H. (2007) Speciation of Fe in silicate glasses and melts by in-situ XANES spectroscopy. *American Mineralogist* **92**, 44–56.

1425 Wilke M., Farges F., Petit P.-E., Brown Jr G. E. and Martin F. (2001) Oxidation state and
1426   coordination of Fe in minerals: An Fe K-XANES spectroscopic study. *American*
1427   *Mineralogist* **86**, 714–730.

1428 Wilke M., Jugo P. J., Klimm K., Susini J., Botcharnikov R., Kohn S. C. and Janousch M. (2008)
1429   The origin of S^{4+} detected in silicate glasses by XANES. *American Mineralogist* **93**, 235–
1430   240.

1431 Wilke M., Klimm K. and Kohn S. C. (2011) Spectroscopic studies on sulfur speciation in
1432   synthetic and natural glasses. *Reviews in Mineralogy and Geochemistry* **73**, 41–78.

1433 Wilke M., Partzsch G. M., Bernhardt R. and Lattard D. (2004) Determination of the iron
1434   oxidation state in basaltic glasses using XANES at the K-edge. *Chemical Geology* **213**,
1435   71–87.

1436 Wilke M., Schmidt C., Farges F., Malavergne V., Gautron L., Simionovici A., Hahn M. and Petit
1437   P.-E. (2006) Structural environment of iron in hydrous aluminosilicate glass and melt-
1438   evidence from X-ray absorption spectroscopy. *Chemical Geology* **229**, 144–161.

1439 Zhang H. L., Cottrell E., Solheid P. A., Kelley K. A. and Hirschmann M. M. (2018)
1440   Determination of $Fe^{3+}/\Sigma Fe$ of XANES basaltic glass standards by Mössbauer
1441   spectroscopy and its application to the oxidation state of iron in MORB. *Chemical*
1442   *Geology* **479**, 166–175.

1443 Zhang H. L., Hirschmann M. M., Cottrell E., Newville M. and Lanzirotti A. (2016) Structural
1444   environment of iron and accurate determination of $Fe^{3+}/\Sigma Fe$ ratios in andesitic glasses by
1445   XANES and Mössbauer spectroscopy. *Chemical Geology* **428**, 48–58.

1446

1447

1448 **Appendix A. Supplemental text and figures**

1449

1450 **Fe-XANES beam damage assessment and corrections, additional figures**

1451
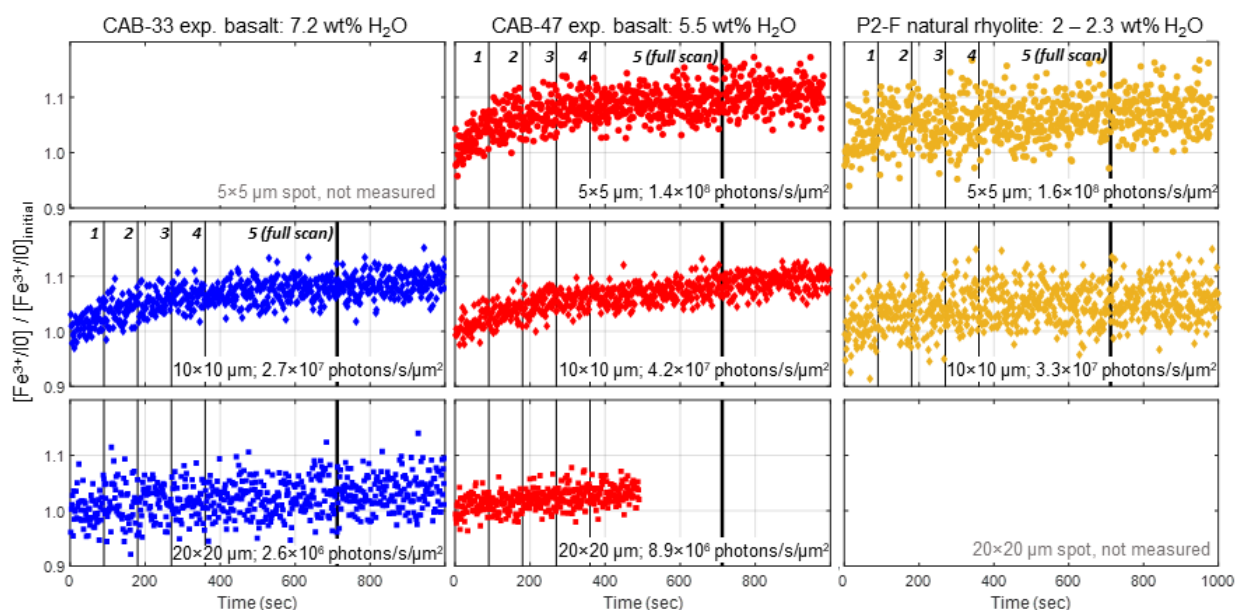
1452

1453 **Figure A.1**. Time dependence of the relative increase of 2nd pre-edge doublet ([Fe-$K\alpha$/I0] / [Fe
1454 $K\alpha$/I0$_{initial}$] at 7113.4 eV, which we consider to be Fe^{3+}/Fe$^{3+}_{initial}$) during irradiation with X-ray
1455 beams of 5×5 μm *(upper)*, 10×10 μm *(middle)*, and 20×20 μm *(lower)* footprint sizes. Fe$^{3+}_{initial}$ is
1456 the average of the first 10 measurements (13 – 15 s of analysis). Thin vertical lines (labeled 1 –
1457 4) indicate analysis end times for repeat pre-edge Fe-XANES analyses (0.5 s/point), as described
1458 in the text. The thick vertical line (labeled 5 full scan) is the end time after the final full energy
1459 scan. Beam damage occurs rapidly in analyses with a focused 5×5 μm beam. However, linear
1460 time-dependent functions can be regressed through the rapid scanning sequence in the first 4.5 –
1461 6 minutes of analyses with 10×10 and 20×20 μm beams to correct beam-damaged induce
1462 oxidation to the initial (t=0 s) conditions. Photon flux densities for analyses with 5×5, 10×10,
1463 and 20×20 μm beams were $1.4 – 1.6×10^8$, $2.7 – 4.2×10^7$, and $2.6 – 8.9×10^6$ photons/s/μm^2,
1464 respectively. We note that experimental glass CAB-33 has a spectral signature that suggests with
1465 the presence of Fe-oxide nanolites (see section **3.1**; **Data supplement**).

1466

1467
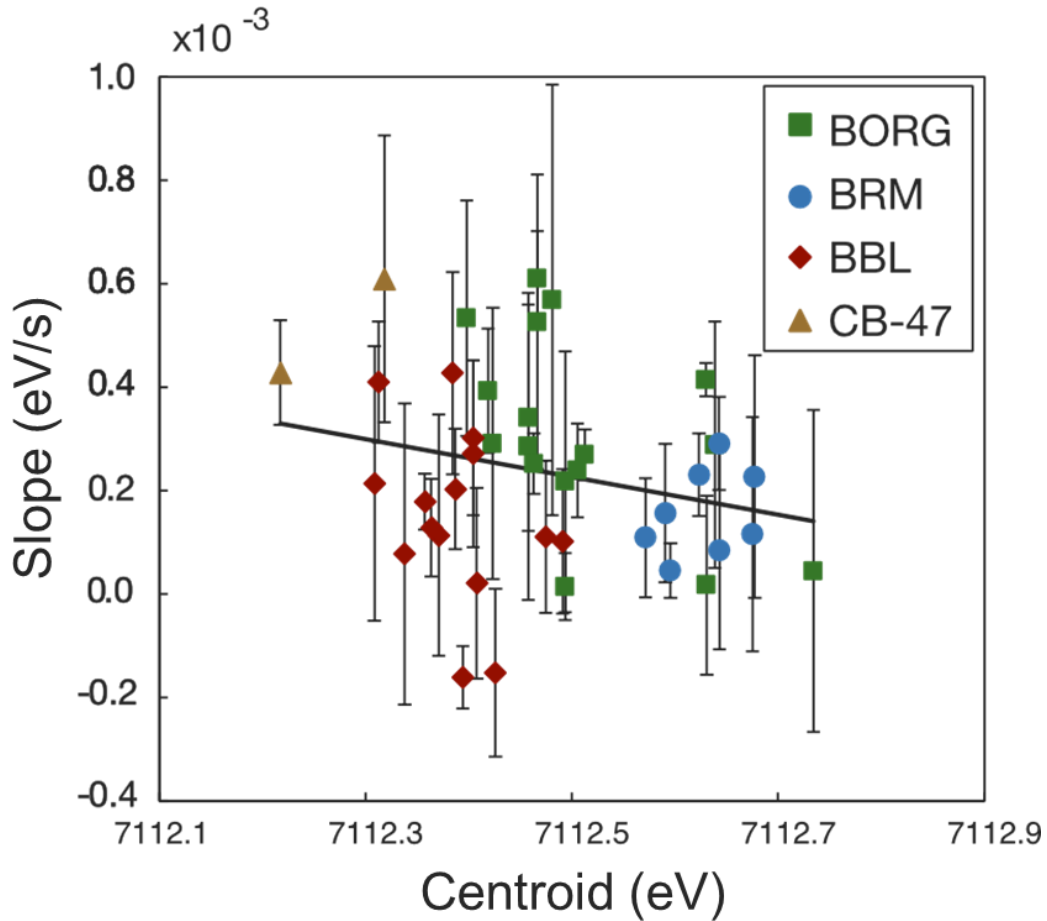
1468

1469 **Figure A.2**. Slopes of linear regressions through Fe-$K\alpha$ pre-edge centroid time series as a
1470 function of the centroid position of the first rapid scan (least affected by beam damage) for
1471 individual samples. The slope of each centroid linear regression can be used as a proxy for the
1472 rate of photo-oxidation. The values of these slopes show an inverse correlation with calculated
1473 initial $Fe^{3+}/\Sigma Fe$ and a positive correlation with H_2O content of each glass (Figure 5), indicating
1474 that beam damage occurs more readily in reduced and/or hydrous glasses (Cottrell et al., 2018).
1475 Although the estimated initial $Fe^{3+}/\Sigma Fe$ is itself dependent on the slope of each regression, the
1476 observed correlation between slope values and $Fe^{3+}/\Sigma Fe$ is not simply an artifact; this plot shows
1477 that the centroid values of the first, least beam-damaged pre-edge scan of each analysis spot
1478 shares the same correlation between t=0 regression slopes and calculated $Fe^{3+}/\Sigma Fe$. Melt
1479 inclusions from three cinder cones in the southern Cascade arc (BORG, BRM, BBL) and
1480 experimental glasses (CAB-47) are grouped by color. Gray line represents linear fit through all
1481 data. All centroids have been shifted by +0.32 eV for consistency with the LW_0 centroid
1482 position reported by Cottrell et al. (2009). See section **2.2** for further discussion.

1483

1484
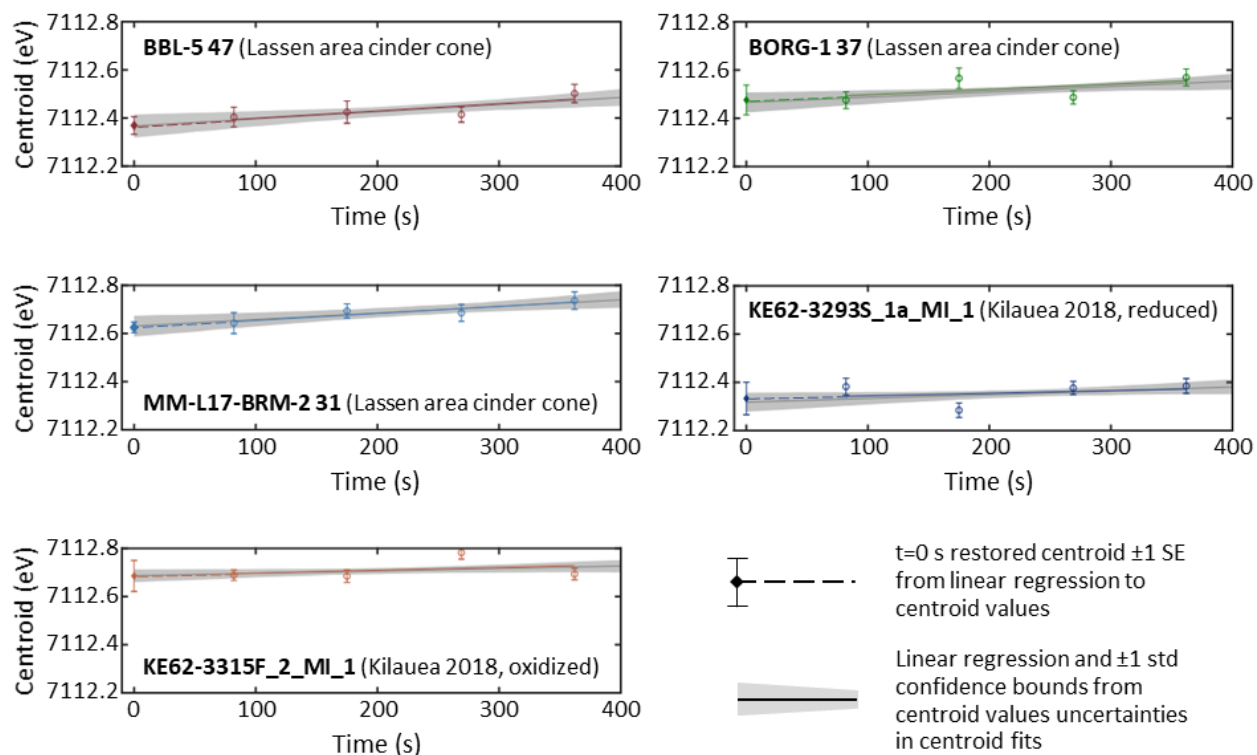
Figure A.3. Fe-$K\alpha$ pre-edge centroid positions calculated from repeated rapid scans of natural melt inclusions shown in Figure 4. Circles represent the centroid values calculated from one pre-edge scan. Error bars represent ±1 SE for individual centroid fits. Colored lines are linear regressions through measured centroid values from 82 to 362 s. Diamonds at t=0 s are the intercept of each linear regression to the centroid time series, and are taken to be the beam damage-corrected initial centroid position. Error bars on corrected initial centroid positions represent ±1 SE of the time series linear regression. Gray bands show ±1 standard deviation non-simultaneous prediction bounds for the linear fit function calculated using a Monte Carlo approach as described in main text. Note that the t=0 s regressions for the H_2O-poor Kīlauea melt inclusions are essentially flat, in contrast to the t=0 s regressions for the more hydrous (and beam damage susceptible) subduction zone melt inclusions from the Lassen area cinder cones.

57
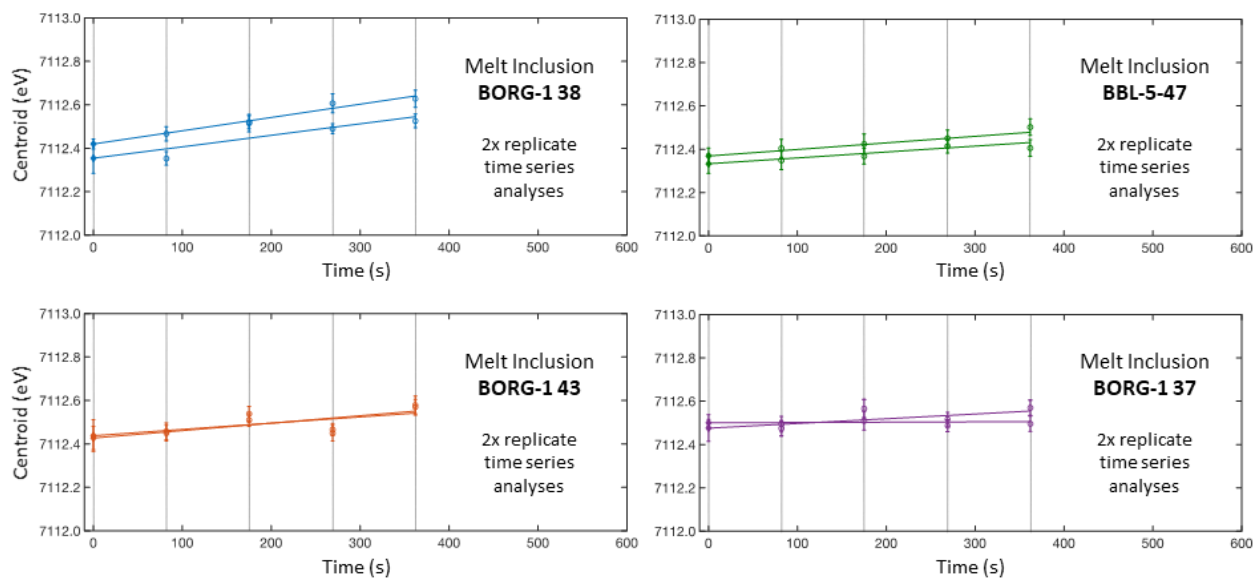
1498

Figure A.4. Centroid positions calculated from replicate sets of rapid pre-edge Fe-XANES scans
within single melt inclusions from the southern Cascades. Analyses were conducted with a
10×10 μm beam and photon flux densities of $3 - 5\times10^7$ photons/s/μm^2. Each sequence represents
repeated measurements in one analyzed spot. Open circles are centroids calculated for each pre-
edge scan. Error bars represent ±1 SE of centroid fits to individual scans. Filled diamonds at t=0
s are the intercept of each linear regression and are used as the time-corrected initial centroid
values. Error bars on the t=0 s centroids represent ±1 SE of each time series linear regression.
Vertical lines indicate analysis end times for repeat pre-edge Fe-XANES analyses. All centroids
have been shifted by +0.32 eV for consistency with the LW_0 centroid position reported by
Cottrell et al. (2009).

S-XANES peak fitting details

Our S-XANES peak fitting approach is calibrated to the suite of experimental hydrous basaltic glasses (45 – 48 wt% SiO_2, 8 – 10 wt% FeO^T, 8 – 10 wt% CaO, 200 MPa, 1050 °C) presented in Jugo et al. (2010) (see **Data supplement**). These glasses were synthesized at different oxidation states and were used by Jugo et al. (2010) to develop an empirical fit relationship of S^{2-} and S^{6+} S-XANES intensities to sulfur speciation. The Jugo et al. (2010) calibration was based on the assumption that sulfur in their most reduced and oxidized end-member glasses occurred entirely as S^{2-} and S^{6+}, respectively, and that linear combination fitting of the end-members produces representative spectra for glasses with mixed sulfur speciation. Using these end-members and linear combination mixed spectra, Jugo et al. (2010) constructed a calibration of S-XANES intensity to sulfur speciation across a range of mixed sulfur states (Figure A.5). We note that the presumed linear combination relationship between end-member sulfur-intensities and sulfur speciation has not been shown independently to be true, but in absence of confirmation from Mössbauer or wet chemistry measurements, it is currently a reasonable assumption and the results agree well with thermodynamic calculations (Jugo et al., 2010).

We use S-XANES spectra for the end-member reduced and oxidized glasses presented in Jugo et al. (2010) to construct linear mixtures of the two and create a S-XANES intensity to sulfur speciation calibration for our peak fitting method (see section **2.3** for details). The main difference between our peak fitting method and the Jugo method is that we isolate the S^{6+} peak from the slightly higher energy ionization peak. By including the ionization peak in our fit procedure, we end up with no S^{6+} intensity in S^{6+}-free glasses, whereas the Jugo et al. (2010) fit method either convolutes the S^{6+} peak with the ionization peak or fits the step-function background differently than we do, which results in ~0.3 $I[S^{6+}]/I\Sigma S$ XANES intensity present in S^{6+}-free glasses. Applying our peak fitting to the full set of hydrous experimental glasses (200 MPa, 1050 °C, FMQ -1.4 to +2.7) presented in Jugo et al. (2010), we find good agreement between sulfur speciation calculated from our method with that of Jugo et al. (2010) (Figure A.8; see **Data supplement**).
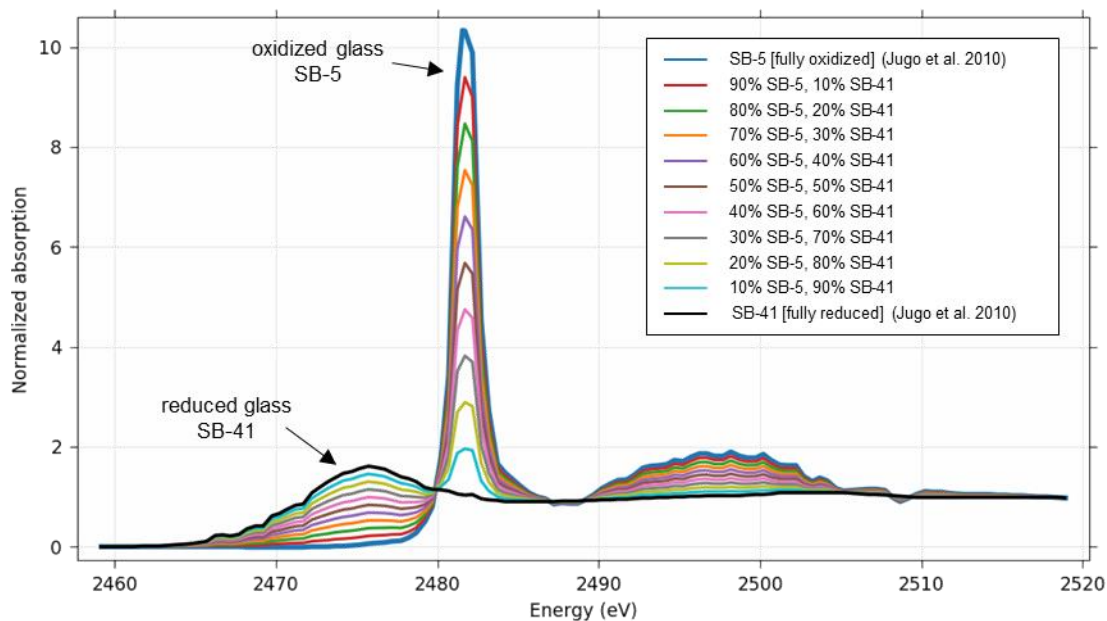
1539

1540 **Figure A.5**. Normalized spectra of completely oxidized (SB-5; FMQ +2.7; $S^{6+}/S\Sigma = 1.00$; blue
1541 curve) and completely reduced (SB-41; FMQ -1.4; $S^{6+}/S\Sigma = 0.00$, black curve) hydrous
1542 experimental glasses reproduced from Jugo et al. (2010) (see **Data supplement**). Linear two-
1543 component mixing of these endmember glasses provides a simulated set of spectra to calibrate S-
1544 XANES intensities to sulfur speciation in glasses in both Jugo et al. (2010) and in the peak-
1545 fitting method presented here. An energy shift of -1 eV has been applied to all the Jugo et al.
1546 (2010) data (see section **2.3.1**).
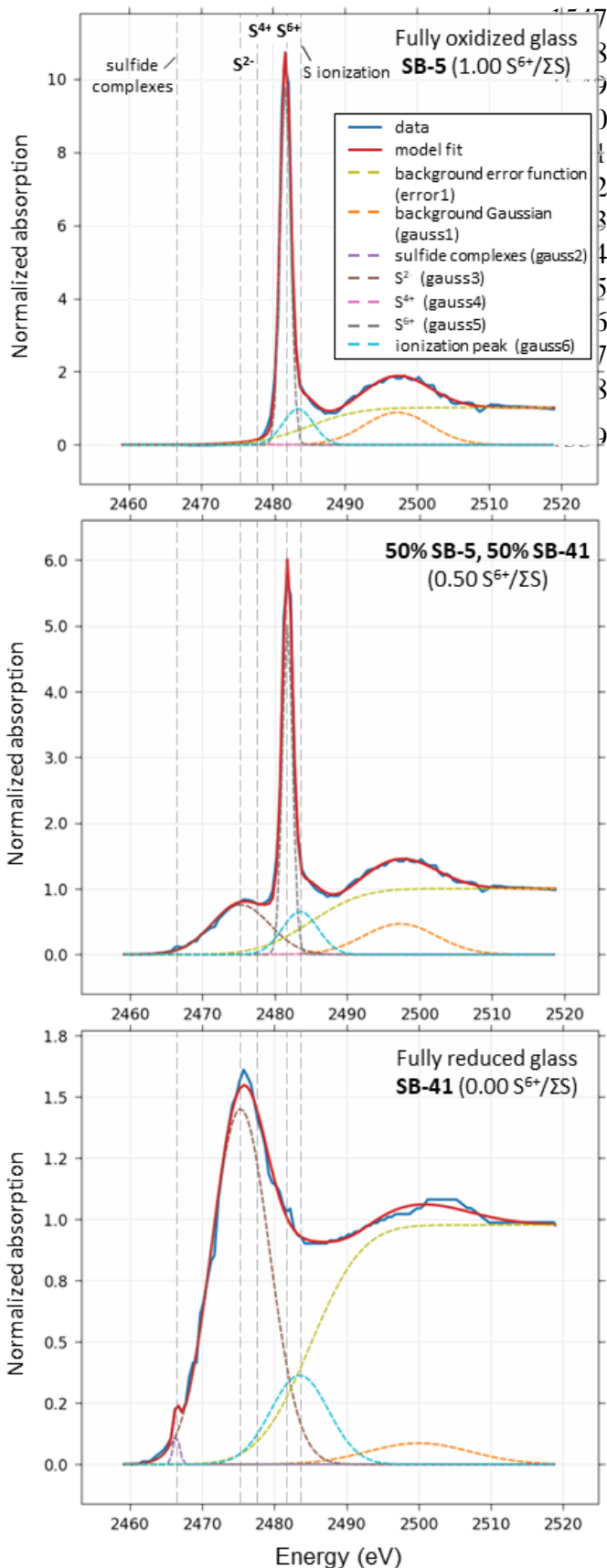
Figure A.6. Example peak fits to the normalized end-member oxidized *(upper)* and reduced *(lower)* hydrous experimental glasses reproduced from Jugo et al. (2010), as well as a 50% linear mixture of the two endmembers *(middle)*. Parameters of the fit functions are identified in Table 2. Reference peak position lines may vary slightly between samples. An energy shift of -1 eV has been applied to all the Jugo et al. (2010) data (see section **2.3.1**).
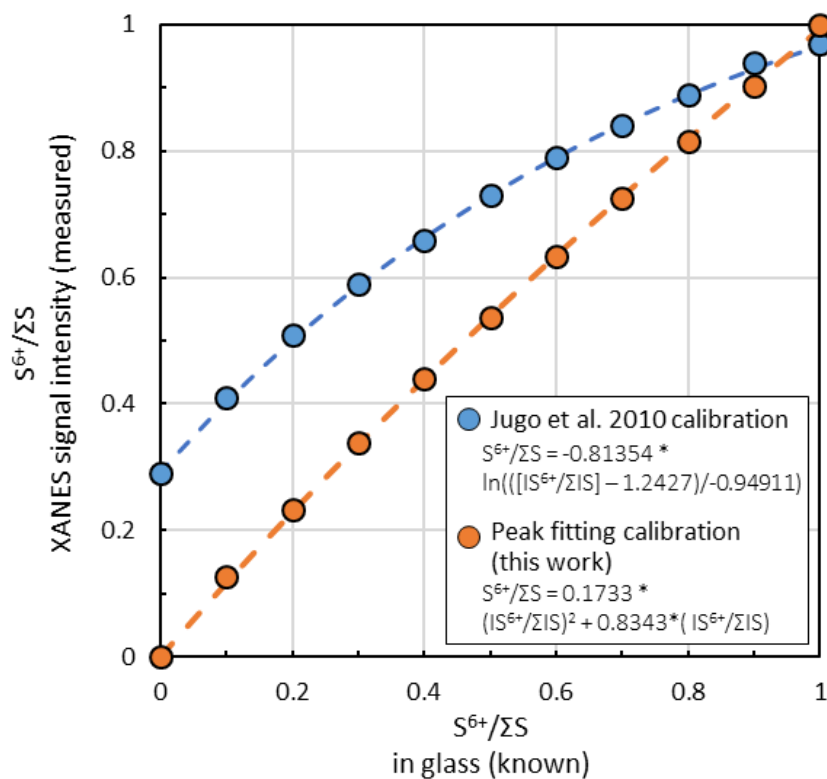
1560

1561 **Figure A.7**. Fit relationships between S-XANES $S^{6+}/\Sigma S$ signal intensity and $S^{6+}/\Sigma S$ speciation in
1562 experimental end-member hydrous glasses and linear component mixtures for the Jugo et al.
1563 (2010) calibration (blue) and the peak fitting calibration in this study (orange). Relative
1564 uncertainties in $S^{6+}/\Sigma S$ signal intensities from S-XANES peak fitting are estimated to be $\pm 7\%$
1565 (2RSE) based on the reproducibility of spectral fitting (see **Data supplement**).
1566
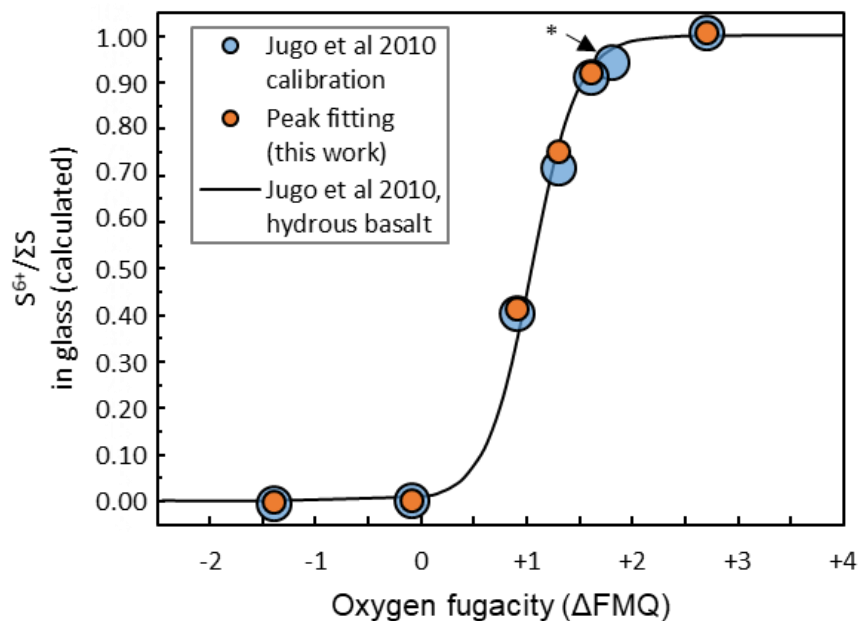
Figure A.8. Calculated sulfur speciation vs fO_2 experimental conditions of the set of synthesized hydrous glasses from Jugo et al. (2010), with XANES spectral fits from our peak fitting method (orange) compared to the Jugo et al. (2010) approach (blue) (see **Data supplement**). Only the most oxidized and reduced glasses were used to calibrate the peak fitting method. Applying our peak fitting method to the Jugo et al. (2010) suite of glass samples synthesized at intermediate fO_2 shows that the two methods calculate very similar $S^{6+}/\Sigma S$ values. Relative uncertainty in $S^{6+}/\Sigma S$ calculations via the peak fitting method is estimated to be ±10% based on the reproducibility of spectra normalization and fitting. The "*" symbol indicates that the normalized XANES spectrum for this glass was not presented in Jugo et al. (2010), precluding inclusion in our comparison. The black curve is the Jugo et al. (2010) predicted relation of fO_2 and $S^{6+}/\Sigma S$ for a hydrous basalt at 1050°C and 200 MPa.

1581 **Appendix References**

1582 Cottrell E., Kelley K. A., Lanzirotti A. and Fischer R. A. (2009) High-precision determination of
1583   iron oxidation state in silicate glasses using XANES. *Chemical Geology* **268**, 167–179.

1584 Cottrell E., Lanzirotti A., Mysen B., Birner S., Kelley K. A., Botcharnikov R., Davis F. A. and
1585   Newville M. (2018) A Mössbauer-based XANES calibration for hydrous basalt glasses
1586   reveals radiation-induced oxidation of Fe. *American Mineralogist* **103**, 489–501.

1587 Jugo P. J., Wilke M. and Botcharnikov R. E. (2010) Sulfur K-edge XANES analysis of natural
1588   and synthetic basaltic glasses: Implications for S speciation and S content as function of
1589   oxygen fugacity. Geochimica et Cosmochimica Acta **74**, 5926–5938.